RESEARCH ARTICLE

ESPL WILEY

Multi-decadal coastline dynamics in Suriname controlled by migrating subtidal mudbanks

Job de Vries[1] | Barend van Maanen[2] | Gerben Ruessink[1] |
Pita A. Verweij[3] | Steven M. de Jong[1]

[1]Department of Physical Geography, Utrecht University, Utrecht, CB, The Netherlands

[2]Department of Geography, University of Exeter, Exeter, UK

[3]Copernicus Institute of Sustainable Development, Utrecht University, Utrecht, CB, The Netherlands

Correspondence
Job de Vries, Department of Physical Geography, Faculty of Geosciences, Utrecht University, Princetonlaan 8a, 3584 CB Utrecht, The Netherlands.
Email: j.devries4@uu.nl

Funding information
NWO, Grant/Award Number: W07.303.106

Abstract

For the development of climate-resilient coastal management strategies, which focus on challenges in the decades to come, it is critical to incorporate spatial and temporal variability of coastline changes. This is particularly true for the mud-dominated coastline of Suriname, part of the Guianas, where migrating subtidal mudbanks cause a cyclic instability of erosion and accretion of the coast that can be directly related to interbank and bank phases. The coastline hosts extensive mangrove forests, providing valuable ecosystem services to local communities. Recent studies on mudbank dynamics in Suriname predominantly focused on large-scale trends without accounting for local variability, or on local changes considering the dynamics of a single mudbank over relatively short time scales. Here we use a remote sensing approach, with sufficient spatial and temporal resolution and full spatial and temporal coverage, to quantify the influence of mudbank migration on spatiotemporal coastline dynamics along the entire coast of Suriname.

We show that migration of six to eight subtidal mudbanks in front of the Suriname coast has a strong imprint on local coastline dynamics between 1986 and 2020, with an average 32 m/yr accretion during mudbank presence and 4 m/yr retreat of the coastline during mudbank absence. Yet, coastal erosion can still occur when mudbanks are present and coastal aggregation may happen in the absence of mudbanks, exemplifying local variability and thus suggesting the importance of other drivers of coastline changes.

The novel remote sensing workflow allowed us to analyse local spatial and temporal variations in the magnitude and timing of expanding and retreating trajectories. Our results demonstrate that it is essential that all coastal behaviours, including changes that cannot be explained by the migration of mudbanks, are included in multi-decadal management frameworks that try to explain current variability, and predict future coastline changes in Suriname.

KEYWORDS
coastline dynamics, Google Earth Engine, mangrove, migrating subtidal mudbanks, remote sensing, Suriname

1 | INTRODUCTION

Coastal wetlands provide a livelihood for local communities and simultaneously provide services that include coastal protection, enhanced carbon storage and habitats provision for both wildlife and ocean life (Kirwan & Megonigal, 2013). Yet, these economically and ecologically important ecosystems, including mangroves, saltmarshes and tidal flats, are under constant pressure from climate change, natural

disturbances and increasing anthropogenic activities (Friess et al., 2012). Variable responses of coastal ecosystems to forcing mechanisms pose challenges for the development of climate-resilient management strategies that need to account for changes in coastal zones that might occur in the coming decades (Dolan et al., 1991).

Mangrove forests are (sub)tropical ecosystems typically located in sheltered coastal environments such as estuaries and tidal embayments, where climatic drivers, tidal currents and sediment dynamics control their distribution, abundance, diversity and dynamics (Osland et al., 2017; Woodroffe et al., 2016; Xie et al., 2020). At the same time, mangroves can also occur along open coasts, changing the forcing mechanisms that determine the long-term fate of these ecosystems compared to sheltered mangrove forests. In such open settings, mangrove forests can expand seaward when waves are low and sediment availability is sufficiently high, or retreat when the opposite is true (Pardo-Pascual et al., 2012). On top of that, variability in coastline positions can occur gradually or episodically, with alternating phases of stability, retreat and progradation (Stive et al., 2002). This is because the driving processes operate at varying spatial and temporal scales, like the redistribution of sediment, anthropogenic interference, sea level rise or hydro-meteorologic forcing mechanisms (Ellison, 2015; Luijendijk et al., 2018).

The coastal zone of the Guianas, stretching from the mouth of the Amazon River to the Orinoco delta in Venezuela, shows exactly this spatiotemporal variability in coastline dynamics (Anthony, Gardel, & Gratiot, 2013; Toorman et al., 2018). Earlier work already linked this to the migration of subtidal mudbanks, consisting of fine-grained sediments that originate from the Amazon River and are transported along the coast (Augustinus et al., 1989; Eisma & van der Marel, 1971). A mudbank is for the most part a muddy subtidal feature, obliquely attached to the coast through its subaerial intertidal extension (Wells & Coleman, 1981b).

Migrating mudbanks are only found in a few places around the globe, including India (Samiksha et al., 2017) and the United States (Taylor & Purkis, 2012). In the Guianas these mudbanks are longer and wider and migrate more quickly; they can therefore be identified by their irregular and triangular shape that can extend up to 20 km offshore and on average 30 km alongshore (Chevalier et al., 2008). Conceptually, where a mudbank migrates alongshore under the influence of waves and currents, coastal accretion can be initiated. This is due to enhanced wave damping and increased sediment deposition near the coastline that is associated with these mudbanks (Winterwerp et al., 2007). Consequently, mud flats form and pioneer mangrove species colonize these flats, further enhancing mud deposition and attenuation of waves (Baltzer et al., 2004; Balke et al., 2011; de Jong et al., 2021). Finally, when the mudbank after 10–15 years has migrated further, the coastline and mangrove ecosystems are again susceptible to enhanced erosion as a result of increased wave activity (Anthony et al., 2010; Toorman et al., 2018).

The conceptual model of mudbank migration has been studied extensively, including field observations of mangrove development and coastline evolution (Augustinus, 2004; Wells & Coleman, 1981a). Also, studies using a variety of publicly available remote sensing observations, including radar, medium-resolution multispectral satellite observations and aerial photographs, show that coastlines of the Guianas are changing due to migrating mudbanks (Baghdadi et al., 2004; Vantrepotte et al., 2013; Walcker et al., 2015). In fact, it

was pointed out that a variety of mechanisms may affect mudbank dimensions, migration speeds and thus coastline changes. Especially waves, but also other controlling factors such as variable trade wind regimes (Augustinus, 2004), the 18.6-year nodal tidal cycle (Gratiot et al., 2008), coastline angle and coastal currents (Lefebvre et al., 2004) are deemed important. This implies a degree of complexity at local scales, going beyond relatively simple alternating phases of erosion and accretion that, despite the attention, are not well understood.

As coastline changes reflect the complex interplay between controlling factors (Boak & Turner, 2005), it is necessary to interpret changes from datasets that have high temporal and spatial resolution, cover large stretches of coastline and go back at least one complete cycle of mudbank migration, including a bank and interbank phase (Li & Gong, 2016). This avoids masking of trends, due for example to changing water levels (Klemas, 2013), and allows capturing subtle local effects within a broader regional context (Almonacid-Caballer et al., 2016). Yet, it also remains challenging to differentiate between subtidal mudbanks, which can extend to intertidal parts of the coastal area, and other coastal landcover classes. Especially when preferred 3D observations, for example from LiDAR, GNSS or terrestrial laser scanners, are lacking or have insufficient spatial and temporal coverage, we rely on two-dimensional interfaces that are visible in images (Moore et al., 2006). In particular, the Landsat archive can be considered a consistent source of long-term observations, with an unprecedented combination of global coverage and a high temporal (16-day return period) and spatial (30 m) resolution (Mondal et al., 2018; Xu, 2018).

The aim of this study is to quantify the effect of mudbanks being present or absent on long-term spatiotemporal dynamics of local coastline changes in Suriname from medium-resolution Landsat imagery. We used an unsupervised decision tree (UDT) that has the ability to extract coastline positions and estimate spatiotemporal differences in mud gradients (de Vries et al., 2021) on the available Landsat images between 1986 and 2020. This series of decisions incorporates a linear spectral unmixing (LSU) model, necessary to estimate sub-pixel coverage of the three dominant types of landcover in muddy coastal ecosystems: water, vegetation and bare consolidated mud. The sub-pixel approach is required because medium-resolution pixels often contain mixed spectral signals, especially in inter- and subtidal regions due to the presence of diffuse boundaries between different land-use classes (Odermatt et al., 2012). This especially hampers the identification of mudbanks in the upper water column, which are rapidly changing as a result of wave climate, tidal flow and river outflow (Zorrilla et al., 2018). Meanwhile it is the detection of mudbanks' presence that is required to separate their effect on coastline changes from other forcing mechanisms.

2 | STUDY AREA

The sparsely populated coastal region of Suriname can be divided into three regions that are intersected by the Suriname River near Paramaribo and the Coppename River (Figure 1). This area receives an average of 2–3 m of annual rainfall, of which most falls in the wet seasons between December–February and April–July. Despite high precipitation, the rivers in Suriname have relatively low discharges
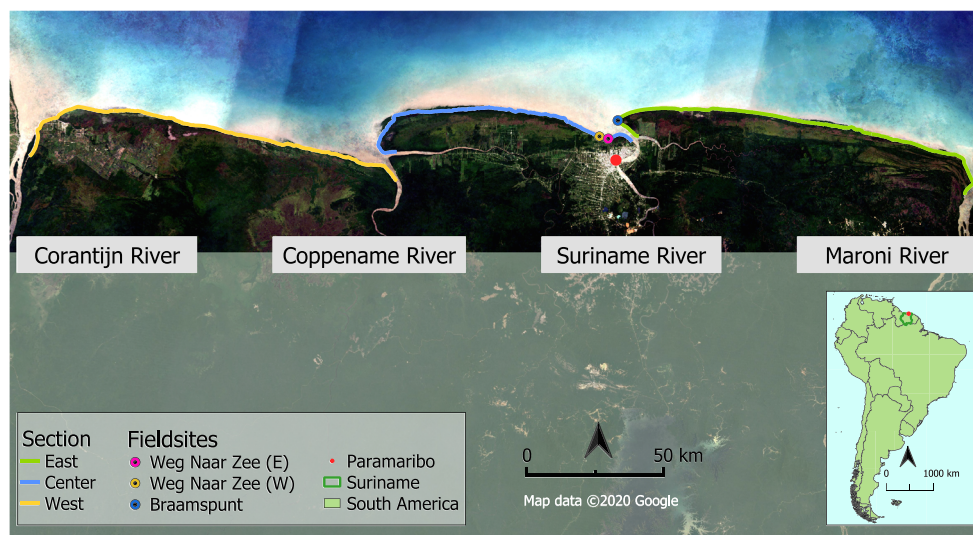
FIGURE 1 The coastal area of Suriname with the different coastline sections. The eastern section is situated between the Maroni and Suriname rivers, the western section between the Corantijn and Coppename rivers, the central section between the Coppename and Suriname rivers. The field sites near Weg Naar Zee (2×) and Braamspunt that are used for the validation are also shown. The image is an RGB median composite of all Landsat observations available between 2017 and 2019, clearly showing the high concentrations of sediment that are associated with the presence of subtidal mudbanks

(∼150 km³/yr) and suspended loads (1–130 mg/L), especially compared to the total alongshore sediment transport and the mud supply originating from the Amazon River (Willems et al., 2015). Nearshore brown waters, between 0 and 20 km offshore, have a high turbidity that can be associated with the suspension of muddy sediments or the presence of mudbanks (Figure 1).

The dominant wind direction at the coast is northeast to southwest during all months of the year. The majority is coming from northeast to eastern directions, with average speeds ranging from 3 to 9 m/s. Relatively stronger winds between December and April coincide with the most energetic offshore waves, up to 2 m significant wave height and periods of 6–10 s (Anthony et al., 2010). This wave-dominated coastal regime shows variations in wave height at timescales ranging from annual to multi-decadal, caused by North Atlantic Oscillation phases and other large-scale atmosphere–ocean interactions (Walcker et al., 2015).

Tides along the coast of Suriname are semi-diurnal, with a micro- to mesotidal scale, ranging from 1.5 to 3 m (Rine & Ginsburg, 1985). The resulting tidal currents are orientated perpendicular to the coastline, which is especially relevant for sediment transport in the mouth of rivers (Augustinus, 2004). All along the coast, the Guiana current runs parallel to the coast, with a velocity varying between 0.2 and 0.6 m/s in the nearshore zone (Pujos & Froidefond, 1995) and between 0.5 and 0.9 m/s outside the coastal boundary (Wells & Coleman, 1981b). The nearshore currents, directly related to residual currents due to wave breaking and tidal flow, contribute to the alongshore migration of mudbanks (Allison et al., 1995; Gratiot et al., 2007). Although coastal dynamics in Suriname are mainly driven by natural processes and interactions between waves, currents, sediment transport and mangrove growth, anthropogenic activities interfere with these natural processes and can locally modify coastal behaviour (Nijbroek, 2014). This includes the building of dikes, removal of mangroves, conversion to agriculture, and the development of aquaculture.

3 | METHODS AND DATA

We studied the spatial and temporal dynamics of the Suriname coastline between 1986 and 2020, in relation to alongshore migrating mudbanks. We therefore first applied a UDT (de Vries et al., 2021) inside the Google Earth Engine (GEE) environment (Gorelick et al., 2017). Afterwards, intermediate outputs from the UDT, consisting of binary land masks and mud abundance maps (Figure 2, steps a–c), were analysed for the presence or absence of mudbank boundaries in relation to estimates of coastline positions (Figure 2, steps d and e). All steps, including a short summary of the UDT, are described below.

3.1 | Pre-processing and UDT

In this work we applied the UDT and subsequent workflow on all top of atmosphere (TOA) images collected over the coastal area of Suriname between 1986 and 2020 by Landsat 4, 5, 7 and 8. These tier-1 products are corrected for atmospheric, illumination and viewing geometry effects, with estimated spatial accuracy sufficient for time-series analysis (Vos et al., 2019).

Due to high cloud cover throughout the year in the study area, the pixel assessment bands were first used to mask out clouds and shadows in all images. To minimize false detection of coastline changes, biased estimates of spectral indices and inaccurate representation in mud abundance maps due to undetected shadows, an additional masking step was implemented (Figure 2, step a). By using the pixels that were initially indicated as clouds and the image metadata describing the solar azimuth, different shadow paths were estimated on a range of pre-defined cloud heights. Within these paths, pixels that reflected low in near infrared (NIR) and two shortwave infrared (SWIR1 and SWIR2) bands were considered shadow pixels (Housman et al., 2018).
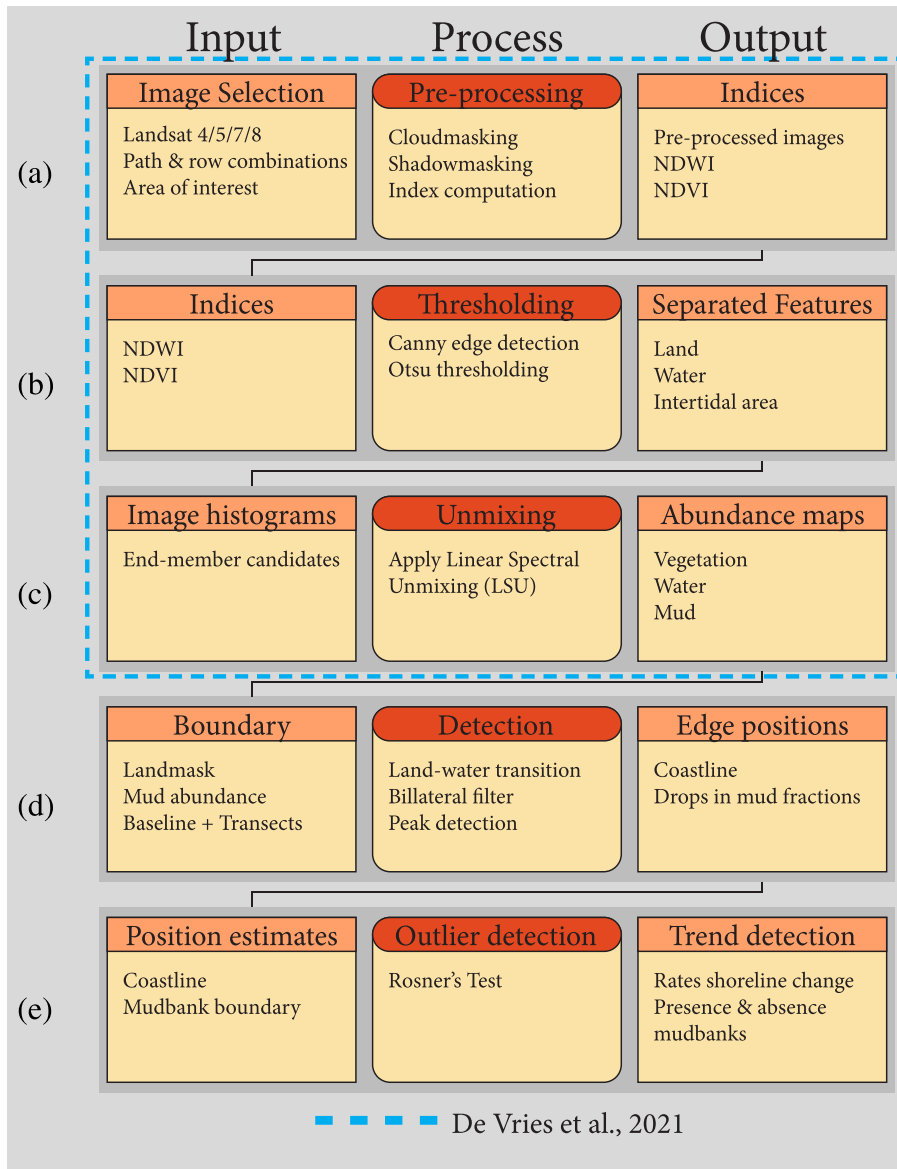
Input Process Output

(a)

Image Selection	Pre-processing	Indices
Landsat 4/5/7/8 Path & row combinations Area of interest	Cloudmasking Shadowmasking Index computation	Pre-processed images NDWI NDVI

(b)

Indices	Thresholding	Separated Features
NDWI NDVI	Canny edge detection Otsu thresholding	Land Water Intertidal area

(c)

Image histograms	Unmixing	Abundance maps
End-member candidates	Apply Linear Spectral Unmixing (LSU)	Vegetation Water Mud

(d)

Boundary	Detection	Edge positions
Landmask Mud abundance Baseline + Transects	Land-water transition Billateral filter Peak detection	Coastline Drops in mud fractions

(e)

Position estimates	Outlier detection	Trend detection
Coastline Mudbank boundary	Rosner's Test	Rates shoreline change Presence & absence mudbanks

– – – – De Vries et al., 2021

FIGURE 2 The applied workflow used to extract coastline positions and simultaneously determine the presence or absence of mudbanks in Landsat observations. The steps from the UDT used are indicated with the blue dashed line (steps a–c). The resulting binary land mask and mud abundance map were then used to estimate the presence of mudbanks simultaneously with the coastline position (steps d and e)

For the non-cloud pixels, the normalized difference water index (NDWI) and the normalized difference vegetation index (NDVI) were calculated as follows:

$$NDWI = \frac{GREEN - NIR}{GREEN + NIR} \tag{1}$$

$$NDVI = \frac{NIR - RED}{NIR + RED} \tag{2}$$

The NDWI uses the reflection in both green and NIR wavelengths to maximize the difference for water features compared to non-water features (McFeeters, 1996). As a result, vegetation and mud usually have low or negative values, whereas water has positive NDWI values. Similarly, the NDVI uses the difference in NIR and red reflectance to indicate vegetated pixels with positive values (Tucker, 1979).

The NDWI was first utilized to detect the interface between land and water (Donchyts et al., 2016). A Canny edge detection algorithm was used to detect local edges based on gradients in the NDWI image (Liu & Jezek, 2004). After filtering these edges on a minimum length,

and buffering the remaining edges, a set of spatial neighbourhoods remained (Figure 2, step b). The bimodal histograms resulting from pixels in these neighbourhoods reflect the difference in spectral properties between land and water that is contained in the NDWI (Donchyts et al., 2016). An Otsu thresholding algorithm was applied to separate these two dominant lobes in the resulting histogram (Lu et al., 2011), to simultaneously separate terrestrial vegetation and bare ground from water pixels, resulting in a land and water mask (Figure 2, step b).

The NDWI and NDVI were then used to detect image end-members required for linear unmixing the fraction cover of mud in each image pixel. Therefore, image histograms, extracted from the Canny edge neighbourhood zones and water masks, were defined to select image end-member candidates (de Vries et al., 2021). By selecting the most abundant NDVI value in the coastal zone, the driest mud pixels in the intertidal zone and the most abundant NDWI value from water pixels, mean spectral signatures were derived for each end-member group. By applying a fully constrained standard linear mixture model, the reflectance signatures were used to derive fractions of landcover type for each pixel in separate bands (Figure 2, step c). These fractions represent the proportion of each active

component to the signal per pixel, with a cover always between 0 (absent) and 1 (full cover) and the sum of all landcover fractions not exceeding 1 (Alcântara et al., 2009).

In order to simultaneously characterize the coastline change rate and mudbank extents along the coastline, transects are defined. As opposed to an area-based method, this transect-based method facilitates analysing rates of coastline change with respect to the presence or absence of mudbanks (Xu, 2018). Therefore, a series of ∼380 transects with a spacing of 1000 m was defined perpendicular to a baseline spanning the coastal zone of Suriname. The baseline is a manually digitized line that is always landward of historic coastlines that are included in the time series of satellite images.

3.2 | Mudbank detection

The presence or absence of mudbanks was determined by detecting abrupt changes in sediment fractions in abundance maps of mud,

resulting from the UDT method (Figure 2, steps d and e). The rationale behind using abrupt changes is that resuspension at the leeward side and deposition at the front side of mudbanks, associated with the migration of mudbanks, results in highly variable mud abundance (Zorrilla et al., 2018). Abrupt changes in mud abundance are thus considered as fuzzy transitions that correspond to diffuse mudbank boundaries. To limit the effect of noise and simultaneously preserve and enhance the changes in sediment fractions in these active migration areas, we opted for a bilateral filtering approach (Figure 3, step 1).

The bilateral filter is a non-iterative technique that uses the weighted average of intensity in nearby pixels, thus taking the local difference in intensity into account while eliminating noise but simultaneously preserving edges (Tomasi & Manduchi, 1998). The filter has two kernels (radius 2): one spatial filter to smooth the image, based on a Gaussian function in the neighbourhood, and a second to highlight the similarity in intensity of the pixel value, compared to other pixels inside the kernel (Asokan & Anitha, 2020):
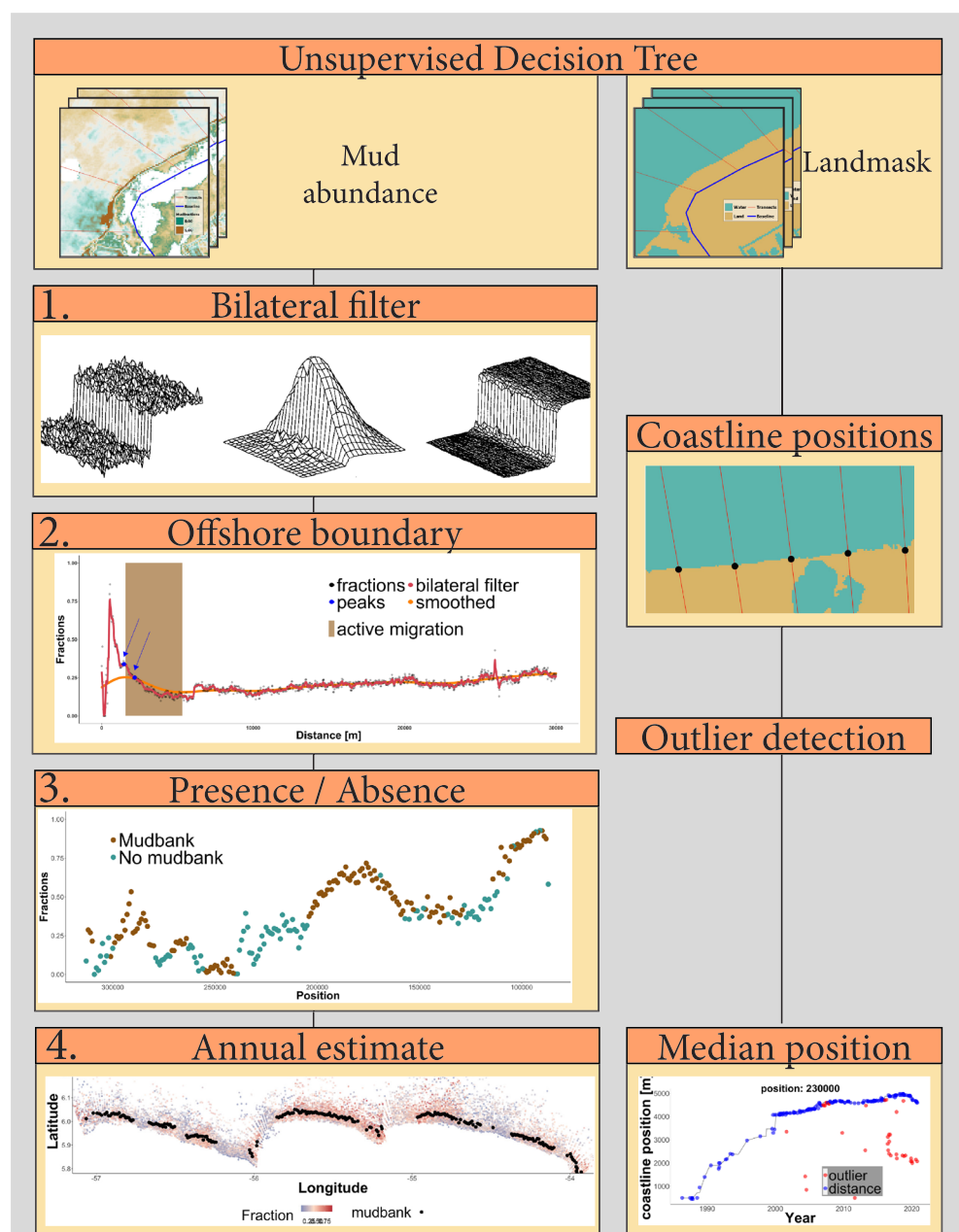

FIGURE 3 The applied steps, following the UDT, to simultaneously determine the exact position of the coastline and the absence or presence of mudbanks. On the right-hand side, the extraction of coastline position and consequential outlier detection to define median annual coastline positions is displayed, as was applied on the binary land masks that resulted from the UDT. Steps 1–4 on the left-hand side show the sequence of steps that were taken to determine the presence of mudbanks for each year from the mud abundance maps that resulted from the UDT

$$l_X(x=p) = \frac{1}{w_p} \cdot \sum_{q \in S} g_s(\|p-q\|) \cdot f_r(l_p - l_q) \cdot l_q \qquad (3)$$

where p represents the selected pixel and q the coordinates in the neighbourhood S, G_s the spatial Gaussian function needed to reduce the influence of distant pixels and f_r the range that reduces the pixels in the neighbourhood when their intensity values differ from pixel p with value l_q. The normalization factor W_p can be computed as

$$w_p = \sum_{q \in S} g_s(\|p-q\|) \cdot f_r(l_p - l_q) \qquad (4)$$

The weight assigned to neighbouring pixels (e.g. with coordinates k, l) to denoise a certain pixel (i, j) can be calculated according to

$$w(i,j,k,l) = \exp\left(-\frac{(i-k)^2 + (j-l)^2}{2\sigma_d^2} - \frac{\|I(i,j) - I(k,l)\|^2}{2\sigma_r^2}\right) \qquad (5)$$

with σ_d (set to 1) and σ_r (set to 5) the smoothing parameters that control the intensity and spatial behaviour of the filter.

The resulting filtered fractions of mud are analysed along each of the intersecting cross-shore transects. In general, these two-dimensional representations show a discontinuous decrease in sediment abundance over the subtidal parts of a mudbank, with abrupt changes being associated with diffuse mudbank boundary (de Vries et al., 2021). Therefore, the smoothed bilateral filter output and a smoothed approximation of the original mud fraction are extracted at each pixel intersecting the transect (Figure 3, step 2). The smoothed approximation is used to define the range of decreasing mud fractions that coincides with this active migration area of subtidal mudbanks, containing the mudbank boundary (Zorrilla et al., 2018). We thereby exclude significant changes in mud fractions that are not related to mudbank boundaries, but to high mud fractions often found in wetlands. Transects with insufficient valid intersecting pixels (<70%), mainly due to clouds and shadows, were also excluded from the analyses.

Within the estimated active migration area, abrupt changes in the mud fractions are extracted from the filtered mud abundance resulting from bilateral output [see Equation 5]. These discontinuities are defined as local maxima that are extracted from the zero crossings of the first-order derivatives of the filtered mud fractions. Local maxima are then selected based on different criteria associated with their fraction value and position along the transect. In this way we ensured that the positions: (1) are farther offshore than the land boundary; (2) are not associated with cloud and shadow remnants; (3) represent an abrupt change in mud fraction; and (4) have a sufficiently high fraction to be associated with mudbanks. Then, for each transect three maxima were selected, associated with the largest absolute decrease, largest relative decrease and quickest decrease (slope), and exported from GEE for further analysis (Figure 3, step 2). These decreases in sediment fraction were considered potential mudbank boundaries as they indicated abrupt changes in mud abundance.

An annual frequency of mudbank presence was computed to compare coastline changes with the presence of mudbanks during a given year. This indication was defined for all transects in individual images. First, we determined along each transect the average increase or decrease in mud abundance. Second, we labelled transects with an offshore increasing mud abundance as no mudbank and excluded the observations concerned from further analysis (Figure 3, step 2). Third, we defined an alongshore-orientated search window and used it to identify local clusters of previously defined abrupt changes, with relatively low mud fractions and thus not considered to be a mudbank (Figure 3, step 3). Finally, a mudbank was considered present when at least 60% of the observations for a given year contained an indication of a mudbank (Figure 3, step 4).

3.3 | Coastline change detection

For each image the binary land mask, resulting from the UDT (Figure 2, step B), was used in this research to extract the last transition from land (1) to water (0) on each individual transect (Figure 3). We then implemented a modified end-point rate method to estimate rates of coastline change from the median coastline distance for a given year, compared to the median distance in the year before (Dolan et al., 1991). By doing so, we avoided omitting important trends in dynamic areas on longer timescales and were still able to separate annual from decadal trends. Even though taking a median value already reduced the effect of random error introduced by our methodology (Boak & Turner, 2005), we applied an outlier test to also exclude systematic erroneous observations (Figure 3).

Systematic errors were mainly related to inaccurate thresholding (Figure 2, step B) and data gaps that result from, for example, clouds, shadows and Landsat 7 ETM Scan Line Corrector (SLC)-off striping. Due to hampered visibility of the actual coastline, when no observation was available, potential false-positive detection of land–water transitions occasionally occurred. These erroneous coastline observations in the time series, measured in metres from the origin of the transect, were removed with the use of Rosner's hypothesis test within time windows of 3 years (Rosner, 1983). The time window was extended by a maximum 2 years when the observation density was lower than 10 observations. This allowed us to detect several unusually large or small coastline distances for each individual transect. The testing is performed in R's EnvStats package (version 2.3.1), with the function *rosnerTest* implemented (Millard, 2014).

3.4 | Coastline validation

Due to the complexity of coastal morphology in muddy coastal areas and the errors associated with the interpretation of coastline proxies from remote sensing images, we opted to compare our coastline estimates with different coastline interpretations (Moore et al., 2006; Li & Gong, 2016). These coastline proxies were manually digitized, based on visual clues in high-resolution orthophotos that we retrieved from different unmanned aerial vehicle (UAV) campaigns. When present, mature vegetation was considered a robust indicator of the coastline (Gratiot et al., 2008). Yet, when vegetation was sparse, the contrast between dry and wet pixels, also referred to as the high water line (HWL), was considered a more suitable indicator (Boak & Turner, 2005). Alternatively, the mean high water line (MHW), a more static estimate, was based on visible features, including cliffs, scarps, washed-up brushwood and human constructions. It is important to mention that these different proxies of coastlines may overlap.

Three orthophotos were created for three highly dynamic sites (see Figure 1): two at Weg Naar Zee and a sandy Chenier at Braamspunt (Anthony et al., 2019). Therefore, we used a DJI Mavic Pro 2 UAV, with a L1D-20C camera model which acquires 20-megapixel photographs that can be used to construct high-resolution orthophotos (Westoby et al., 2012). We collected these photographs at different flying heights with a forward and side overlap of 80 and 60%, respectively (Table 1). During low tide, six to nine separate flights were planned and executed in Litchi software, aimed at collecting alternating nadir and off-nadir pictures to minimize doming (Carbonneau & Dietrich, 2017). Markers and natural terrain features, measured with Emlid Reach+ RKT GPS, were used as ground control points to process the photographs in Agisoft Metashape version 1.5 into point clouds and ultimately orthophotos with a downscaled resolution of 50 cm. The accuracy of these orthophotos ranged between 0.02 and 0.1 m (Table 1), substantially smaller than the uncertainty associated with the acquisition of Landsat images.

Satellite images taken within 100 days of the orthophoto acquisition date were considered for validating the coastline position. This selection resulted in 12 unique satellite images for which coastline positions were estimated, following the procedure described in previous sections (see Figure 3). As opposed to using transects with 1000 m spacing like we did for the entire coast of Suriname, we used transects with a spacing of 50 m for the validation. Euclidean distances between the resulting position estimates and the different manually delineated coastline proxies (vegetation interface, MWL and MHW) were calculated as indicator for the overall accuracy of position estimates.

4 | RESULTS

4.1 | Mudbank dynamics

The alongshore variation in mud fractions can be associated with the presence or absence of six to eight mudbanks of varying length in front of the Suriname coast between 1986 and 2020 (Figure 4). Especially in the western part of Suriname, between 0 and 120 km, three or four clearly distinguishable alongshore migrating mudbanks can be seen. Also, in the middle section it is possible to distinguish segments associated with the front of one migrating mudbank between 2000 and 2010. Finally, in the eastern section, two segments that are associated with mudbanks are visible. All these segments show a clear shift from east to west, associated with their migration direction and speed. The seemingly smaller east-to-west shift for each segment between different years in the western sector, compared to the middle and eastern parts of Suriname, suggests slower migration rates of mudbanks towards the Corantijn River (Figure 1).

In general, high mud fractions, ranging from ∼0.4 to ∼0.8, indicate the presence of mudbanks because continuous transport of mud towards the front of mudbanks causes a higher turbidity. Mud at the

TABLE 1 Characteristics of the different surveys, including the XY error representing the average horizontal offset computed from a set of independent ground control points (*n*). The Landsat images column indicates the number of Landsat images that are validated with the corresponding orthophoto

Date	Location	Substrate	Images (flights)	Flying height [m]	Area [km²]	XY error [m]	Landsat images [n]
2019-06-20	Weg Naar Zee (W)	Mud	1102 (6)	50	0.51	∼0.02 (n = 21)	8
2019-07-13	Weg Naar Zee (E)	Mud	1192 (6)	30	0.21	∼0.02 (n = 13)	5
2019-07-24	Braamspunt	Sand	1188 (9)	75	1.16	∼0.1 (n = 10)	6
2020-02-19	Weg Naar Zee (W)	Mud	1385 (9)	75	0.63	0.04 (n = 9)	3
2020-03-03	Braamspunt	Sand	885 (8)	100	0.73	0.06 (n = 37)	4
2020-03-04	Braamspunt	Sand	478 (6)	100	0.63	0.02 (n = 22)	4

FIGURE 4 Mean values of the peaks of mud fractions and position estimates of mudbanks, distributed along the coastline of Suriname for all years between 1986 and 2020. The peaks of sediment fractions were calculated as described in the text and Figure 3, step 2. The presence of mudbanks was estimated for each transect based on the steps explained in the text and Figure 3, step 3. Masked-out values are related to transects that are in the mouth of the Suriname and Coppename rivers (Figure 1) or missing satellite data
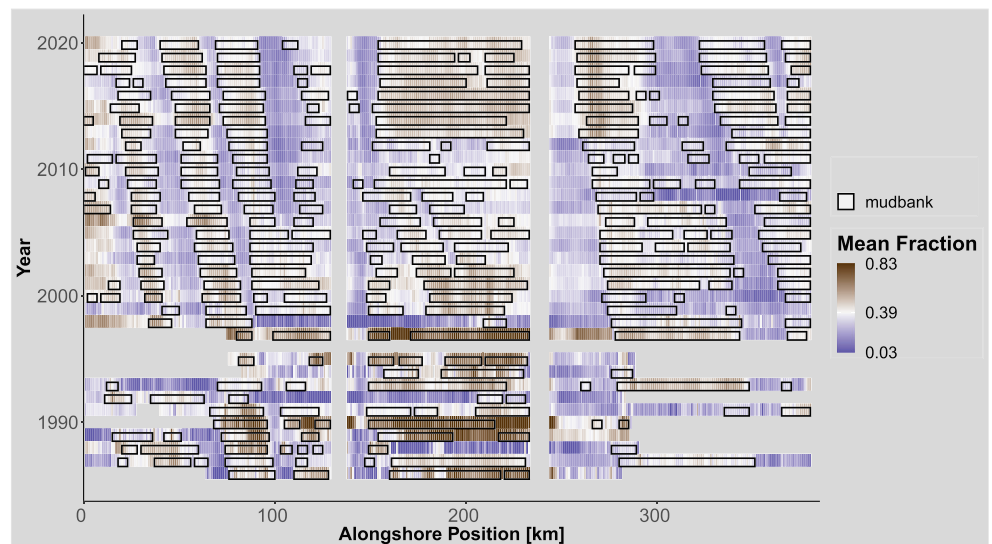
coast, especially near the back of mudbanks and in the interbank zones, is consolidated and therefore not easily resuspended, causing lower mud abundances in the water column (Vantrepotte et al., 2013). This can, for example, be illustrated by the band of lower mud fractions (∼0.05 and ∼0.3) in the eastern sector between 300 and 350 km (Figure 4).

4.2 | Validation of coastline position

Coastline positions, derived from Landsat images, are compared to different coastline interfaces digitized in the UAV images acquired over Weg Naar Zee at 2019-06-20 (Figure 5, panel A). Coastline positions retrieved from the Landsat images that were acquired 72 days (2019-08-31) and 80 days (2019-09-08) after the UAV acquisition date (2019-06-20) show significantly larger mean distances compared to the digitized coastlines (Figure 5, panel b).

We developed similar comparisons between the automatically derived coastline positions in all the selected Landsat images and the defined coastline proxies in the different high-resolution UAV images (see Appendix A, Figures A1–A4). Overall, position estimates agree with the observations, indicating on average <50 m distance (<1.67 Landsat pixels) to the different reference lines (see Appendix A,

Figure A5). The median Euclidian distance from each coastline position to the nearest line is <30 m. The coastline position estimates predominantly agree with the lines corresponding to the MHW and HWL (see Appendix A, Figure A6). Exceptions are the MHW acquired in the Weg Naar Zee UAV image of 2020-02-19 and the vegetation interface acquired at Braamspunt in 2019-07-2 (Figures A2 and A3). Comparisons between Landsat-derived coastline positions and the coastline proxies retrieved from the UAV images acquired over Braamspunt show 8–12 significant outliers, with distances of up to 600 m. These offsets can be attributed to the spit that has formed, with a width sometimes smaller than the size of one Landsat pixel (Figure A4).

4.3 | Coastline dynamics

The annual rate of coastline changes between 1986 and 2020, in relation to the presence of mudbanks in front of the Suriname coastline, is shown in Figure 6 (panel a) and video S4. Of all coastline position changes, 90% range from −125 m/yr of erosion to 150 m/yr of accretion. Overall, there are no clear trends with dominant accretion or erosion rates between 1986 and 2020 for the entire coastline (Figure 6, panel b). Yet, years of erosion and
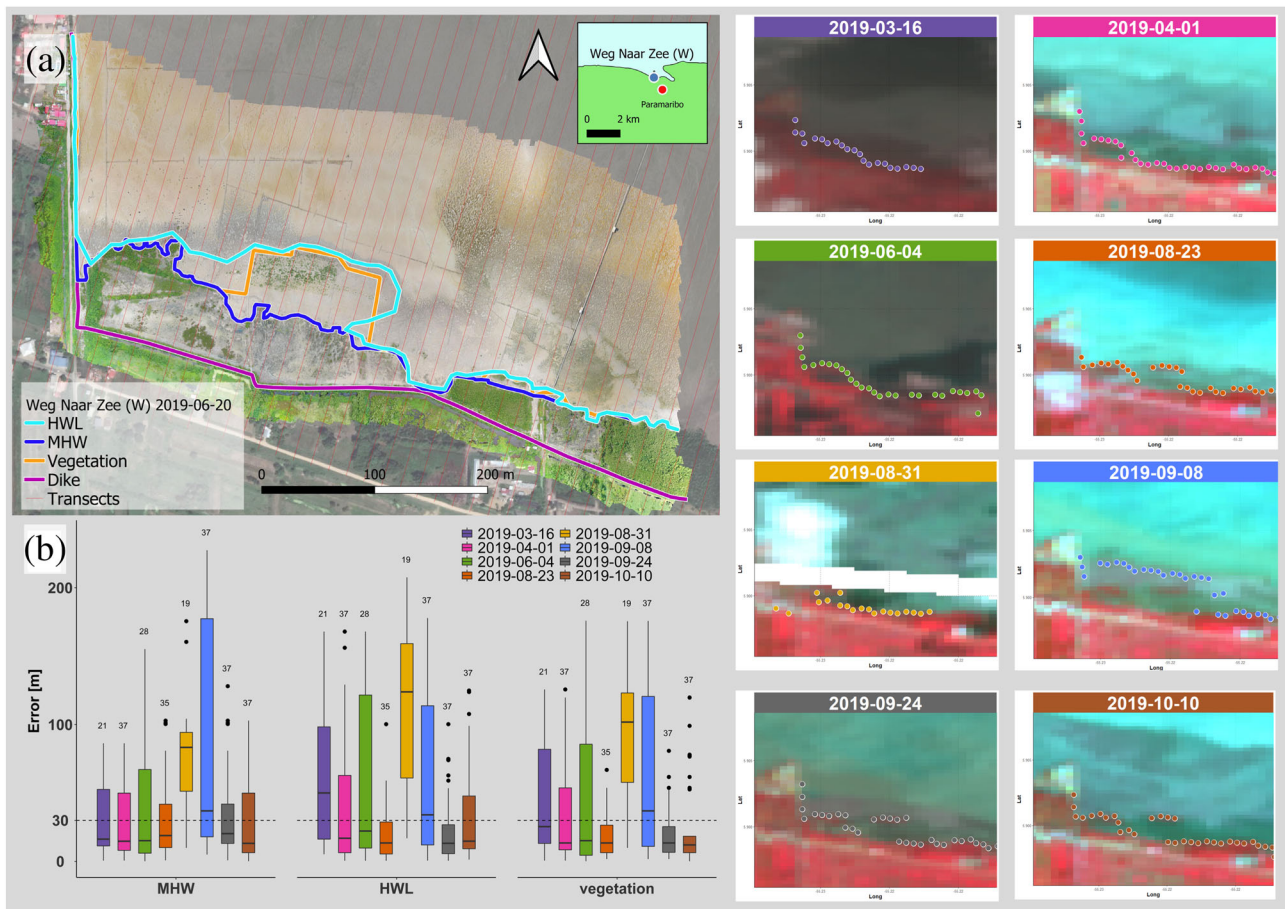

FIGURE 5 Validation results of the Landsat images acquired within 100 days of the high-resolution UAV campaign near Weg Naar Zee west (2019-06-20). Panel a shows the digitized shorelines in the UAV image that are used for validation. The panels on the right show the different Landsat images that are used, together with their automatically derived shoreline positions. The coloured boxplots in panel B summarize the difference for each of these Landsat-derived shoreline positions compared to the different digitized shoreline positions visible in panel A (MHW, HWL and vegetation interface). The Landsat 7 image acquired at 2019-08-31 shows missing data related to SLC-off striping
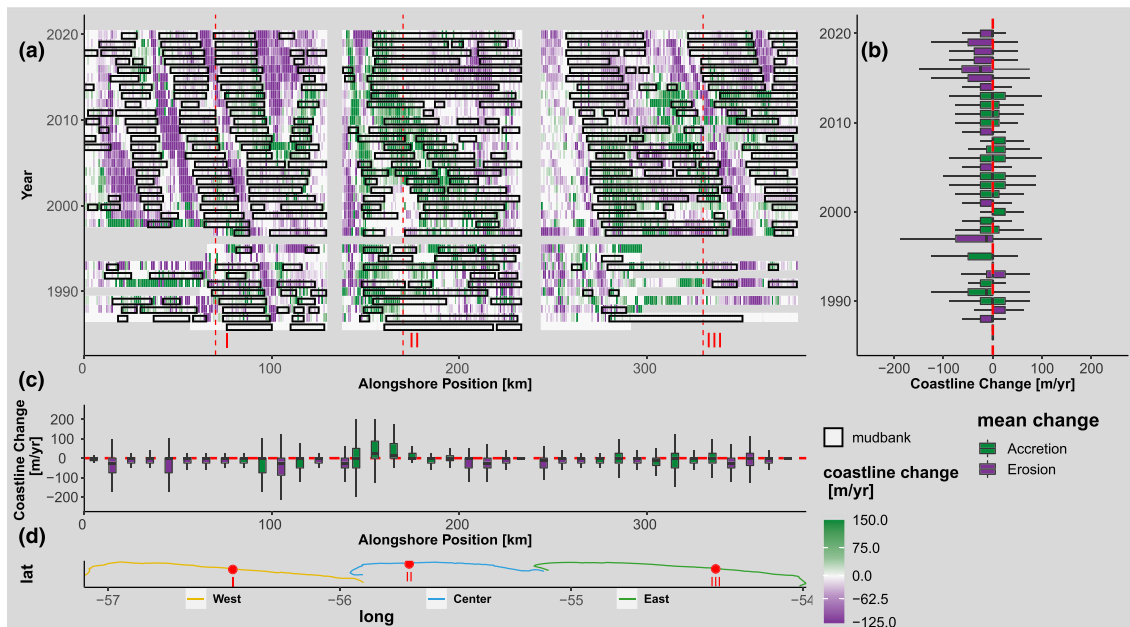
FIGURE 6 The presence and absence of mudbanks in relation to observed coastline changes in Suriname between 1986 and 2020 (panel a). Panel b shows ranges of annual coastline changes, where green indicates mean accretion and purple mean erosion for the given years. In panel c, the alongshore distribution of coastline changes is given for every 10 transects. Panel d shows the coastline of Suriname with the coastal sections indicated by east, centre and west. The positions of the selected example transects are indicated with I, II and III. Note that the x-axis of panel d (in units of longitude degrees) is not the same as the x-axis of panels a and c (in units of alongshore distance)

FIGURE 7 Changes occurring in coastline position between 1986 and 2020 in the eastern, central and western sections of the Suriname coastal area (Figures 1 and 6). The y-axis values correspond to the number of observations in each bin of normalized coastline position estimates. The solid and dashed lines indicate the mean values for each section and the entire coastline, respectively. For each transect, all coastline positions are compared to the first observed valid coastline observation
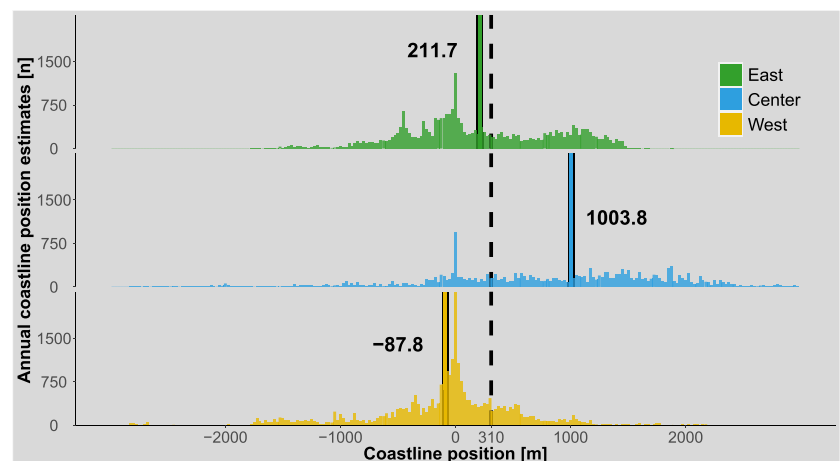
accretion are alternating, with on average erosion in the last 7 years (2014 - 2020). Especially in the western region (Figure 6, panel c), alternating zones with on average accretion or erosion are visible, although no single transect shows continuously erosion or accretion for the studied period 1986–2020.

Figure 7 supports the general observation that Suriname has an accreting coastline with an averaged total of 310 m between 1986 and 2020, yet there is strong alongshore variability. More specifically, the western section is characterized by erosion, with a mean coastline position change of 88 m, but also with occasional accretion compared to 1986. The eastern section has an average accretion in coastline position of 212 m compared to 1986. Finally, the middle section shows overall accretion for each transect, with an average coastline change of 1004 m compared to 1986. For the studied period, a significant part of the total accretion in Suriname

occurs in the central region, with the majority of it between 2002 and 2011. From the year 2000 onwards accretion reduces, first from km 200 and then shifting in the western direction (Figure 6, panel a).

Both accretion and erosion occurred at relatively local scales (i.e. difference in order of magnitude change within 10–30 km alongshore distances; Figure 6, panel a). This suggests that spatial zones can be defined, where either accretion or erosion of the coastline was dominant in a specific period (Figure 6, panel c). For each year, inversion points along the coastline can be seen where this accretion changes to erosion or vice versa (Figure 6, panel a). Not only do these inversion points mark the accreting zones under influence of mudbanks, but their position changes between years are a good indication of migrating mudbanks (Froidefond et al., 1988).

Examples of variability in these inversions at local scales are visualized in Figure 8, where the coastline position in the eastern region (transect III, panel c and video S3) changes from roughly 100 m in 2002 to almost 1350 m, 2 years later, and eventually ∼1100 m in 2009. A mudbank was already present from 1997 and completely passed in 2009. From 2009 the coastline eroded slightly to 1200 m, with stabilization from 2015 onwards. Also, between 160 and 230 km alongshore a phase of coastal accretion can be observed, with occasionally accretion rates surpassing 150 m/yr (Figure 6, panel a). As

opposed to transect III, the accretion of the coastline for this location (transect II, Figure 8, panel b and video S2) starts within 1 year of the arrival of a mudbank. Also, between 275 and 400 km alongshore, westerly deflecting strips of accretion are clearly distinguishable (Figure 6, panel a). Under the influence of a mudbank, the coastline remains stable between 1999 and 2004, with rapid accretion of ±300 m until 2011 (transect I, Figure 8, panel a and video S1). Then erosion rates rapidly go up to, or sometimes even surpass, 125 m/yr between 2012 and 2015, followed by stabilization of the coastline and the appearance of a new mudbank in 2018. These differences in the magnitude and timing of coastline responses to appearing mudbanks exemplify the spatiotemporal variability present in the system.

Overall, accretion zones coincide with the presence of mudbanks, and erosion zones can be linked with the absence of mudbanks (Figures 4 and 6a). As supported by Figure 9, mudbanks tend to be associated with accretion rates of 32 m/yr. Vice versa, the absence of mudbanks is in general associated with mean erosion rates of 4 m/yr. The difference between the two skewed groups (Shapiro–Wilk test, p-value < 0.0001) of coastline changes, affected by the presence or absence of mudbanks (Figure 9), is significantly different (Wilcoxon rank test, p-value < 0.0001). Relatively smaller erosion rates are also observed when a mudbank is present, or moderate accretion rates when a mudbank is absent.
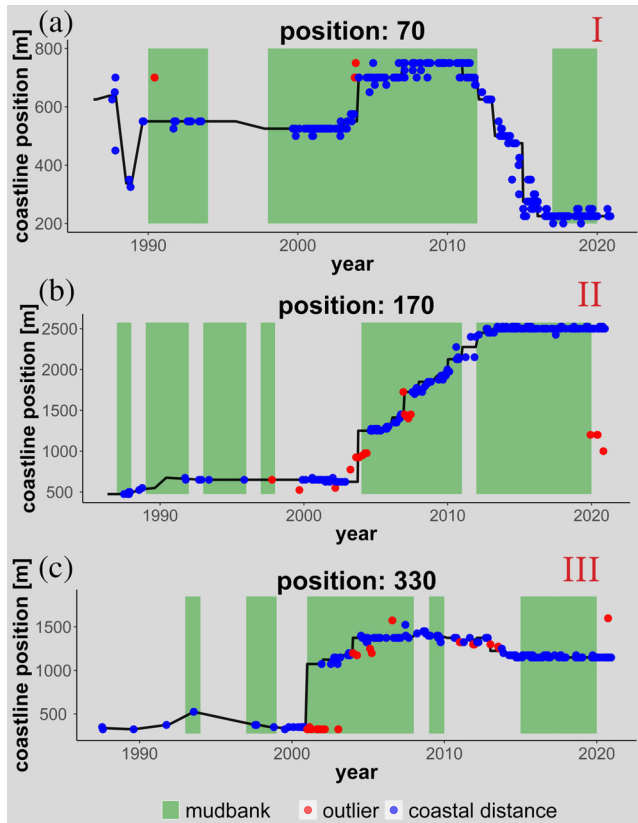
5 | DISCUSSION

5.1 | Mudbanks

Our semi-automatic methodology allowed us to visualize the alongshore variation in mud abundance between 1986 and 2020, link it to the presence or absence of mudbanks, and identify likely mechanisms that dominate nearshore variations (Figure 4). The satellite-derived estimates of mud abundance in shallow waters indicated the presence of six to eight migrating mudbanks along the coast of Suriname. These mudbanks show strong spatial and temporal variations mud abundance. Previous research already coupled the local variation of mud abundance in the upper water column to active resuspension and migration of an individual mudbank (Vantrepotte et al., 2013; Zorrilla et al., 2018).
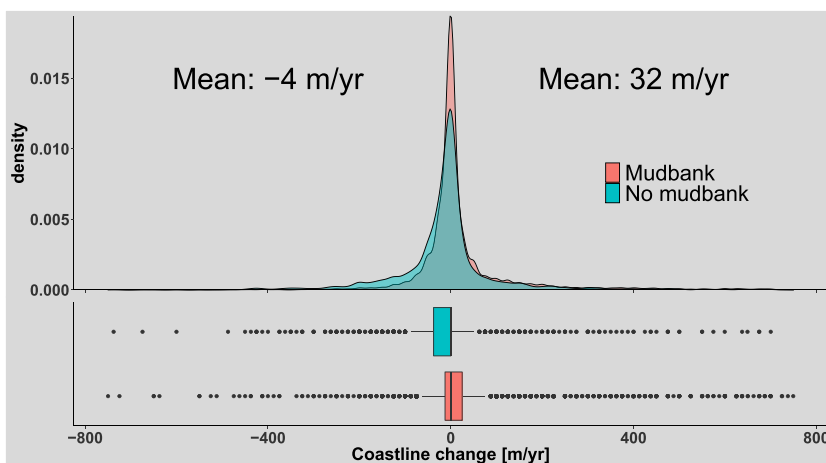

FIGURE 8 Development of the coastline position between 1986 and 2020 of the three transects (I, II and II) indicated in Figure 6. Coastline position is expressed as distance of the last land–water transition compared to the origin of the transect. The median values are connected by the black line. Note the different y-axis ranges for each subplot

FIGURE 9 Annual rates of coastline change between 1986 and 2020 for transects that are either fronted by a mudbank or not. The distribution of change is indicated by the density plots and the median, interquartile ranges and outliers are indicated by the boxplots in the bottom panel. For visualization purposes, the x-axis range is limited to −800 to +800 m/yr

Variations in mud fractions clearly exist when looking at multiple mudbanks simultaneously at different moments in time. This illustrates the link between the changes in the footprint of mudbanks that are visible in remote sensing images and variability in hydrodynamic forcing mechanisms such as waves, tides, currents and river flow (Orseau et al., 2020). This is because so-called wave–bank interactions constantly affect the migration rate, shape and mud budget of these banks (Anthony, Gardel, & Gratiot, 2013; Gardel & Gratiot, 2005). This suggests that spatiotemporally variable mud fractions can be associated with the presence or absence of a mudbank. Also, within the footprint of these mudbanks, variable mud fractions are observed (Figure 4), probably associated with wave–mud interactions that control resuspension at the leeward and deposition at the front side (Zorrilla et al., 2018). This not only limits the use of generic thresholding on sediment fraction or concentrations to separate mudbanks from their surroundings, but also indicates that these interactions enhance variability between separate mudbanks and consequential coastline dynamics.

5.2 | Implication for foreshore changes

For the first time we were able to identify hotspots of contrasting behaviour, overall trajectories of coastline change and related to these, the presence or absence of mudbanks (Figures 4 and 6). In general, the Suriname coast accretes with an average of 32 m/yr when a mudbank is present (Figure 9), comparable to the previously reported range of 13–100 m/yr in French Guiana (Plaziat & Augustinus, 2004). Occasionally rates up to 400–800 m/yr were detected (Figure 6), which is significantly higher than the previously reported upper limit of 200 m/yr (Allison et al., 2000; Augustinus, 2004; Proisy et al., 2021). We show that the coast erodes by 4 m per year on average under mudbank absence, reaffirming that coastal erosion prevails when a mudbank has migrated further alongshore and no longer protects the coast against incoming waves (Allison et al., 1995; Anthony et al., 2010; Gardel & Gratiot, 2006).

Coastline positions in the different sections along the coast of Suriname showed variable responses to the presence or absence of mudbanks, between 1986 and 2020 (Figure 7). One explanation for the regional difference comes from cheniers, sand ridges created by sand supplied from local rivers, such as the Suriname and Corantijn rivers, together with winnowing of sand from deposits by constant wave reworking. Especially in the western sector the cheniers, if present at all, are smaller and thus provide less protection against erosion than in the east (Augustinus et al., 1989), potentially explaining the difference in erosion.

Exceptional accretion rates in the central section of Suriname suggest, however, that this is at best only part of the explanation (Figures 7 and 8, panel b). Observerd changes in the orientation of coastlines and the presence of sufficiently large coastal features, such as mudscapes and small islands, provide shelter against incoming waves and might even promote accretion. Together with the slowing down of the mudbank approaching the mouth of the Coppename River from 2008 onwards (Figure 6, panel a), caused by the hydraulic groyne effect (Anthony, Gardel, & Gratiot, 2013), this might explain the enhanced sedimentation and coastline accretion east of the river mouth (∼km 140). Consequently, sediment deposition downdrift becomes limited, thus promoting enhanced erosion west of the river mouth (∼km 100), starting from 2013 onwards (Figure 6, panel a). This example clearly highlights the difference in coastline response to a passing mudbank, but also the different magnitude of changes induced by a single mudbank on different stretches of coastline with the passing of time.

Our results further highlight the episodic, rather than uniform, nature of the coastline position changes on local scales, with rapid coastline accretion and retreat as response to changes in forcing mechanisms, including mudbank migration (Augustinus, 1989). Yet, variability in timing can occur, as coastal accretion can immediately follow the arrival of a mudbank (Figure 8, panel b), lag several years (Figure 8, panels a and c) or not happen at all. This again emphasizes the importance of other factors such as the variation in topography of the intertidal area (Anthony et al., 2008; Proisy et al., 2009). As a result, differences in submersion time, flooding frequency and drying–wetting cycles cause mud cracks and development of mud bars, altering conditions for successful seed trapping and thus mangrove growth (Gensac et al., 2011).

Previous research has shown that shoreline trends lasting multiple decades occur, as opposed to the alternating phases of accretion and erosion that the conceptual model of migrating mudbanks describes (Fromard et al., 2004; Plaziat & Augustinus, 2004). Our results (see Figure 6, panel a) can now indicate where erosion, despite the presence of mudbanks (e.g. around km 350 after 2012), and accretion can occur, even when mudbanks are absent (e.g. km 150). The former are examples of potential new shoreline trends of prolonged and persistent erosion, due for example to polders or mangrove removal (Brunier et al., 2016). Also, observations of mudbanks not promoting coastal accretion (e.g. km 35 and 180), despite enhanced wave damping, suggest additional factors are playing a role in successful mangrove colonization and establishment. Previous research indicated that this can be related to reduced material exchanges between mudbanks and shorelines, especially at leading and inner edges of mudbanks (Anthony, Gardel, Proisy, et al., 2013). This streaming of mudbanks, a process where mudbanks are disconnected from the shoreline, results in reduced material exchange, smaller intertidal mudflats and thus less accommodation space for mangrove colonization and coastal accretion (Gensac et al., 2011; Proisy et al., 2009). It is estimated that these long-term processes may involve local changes in wave–bank interactions as well as coastal mud budget adjustments alongshore (Anthony, Gardel, Proisy, et al., 2013).

In general, we can see that the extent to which the shore-welded part of a mudbank is preserved from erosion in interbank phases determines the degree of coastal progradation in the following mudbank phase (Allison & Lee, 2004; Anthony et al., 2010). However, complex patterns of erosion and accretion confirm again that the coastline positions and their trajectories are not only influenced by mudbank dynamics. The average erosion or accretion rates should therefore be considered more as a mid-term (e.g. one full mudbank cycle) tendency on local to regional scales, rather than a definitive indicator of what may happen on a longer timescale. Yet, additional research on the extent of intertidal areas and factors that control successful mangrove colonization, in relation to forcing

mechanisms such as wind-wave regimes (Augustinus, 2004) and currents, is required to quantify the potential impact of each individual aspect.

5.3 | Coastline accuracy

The different coastline definitions, namely HWL, MHW and the vegetation interface, as mapped in the high-resolution UAV imagery (Figures 5 and A1–A4), are in good agreement with the coastline position estimates. These estimates from 12 Landsat images, acquired within 100 days of the UAV acquisitions, are on average within 50 m of the reference lines (Figure A5). Disparities in error between the Landsat observations and the different coastline proxies exemplify the uncertainty associated with the selected point-based method for estimating coastline position from land–water transitions along a transect. This method is a computationally efficient way of analysing spatiotemporal variation in coastlines, yet the accuracy depends on the orientation and location of the transects, as the spatial context of the coastline estimate is one dimensional. As a result, information from adjacent pixels is not incorporated in the estimation of coastlines, resulting in the potential detection of incorrect land–water transitions. Variation in the average error for the different UAV images also represents the difficulty in consistently mapping land–water boundaries over complex, heterogenous landscapes. This can be seen, for example, in the larger error estimates of Braamspunt, a sandy chenier with relatively complex landcover and coastline shape, compared to the two sites at Weg Naar Zee (Figure A6).

When the true coastline position cannot be determined due to missing data, offsets in accuracy can be large. This is, for example, indicated by the outliers found in the Braamspunt UAV images (Figures A3 and A4). As the most seaward land–water transition is obstructed from sight by clouds, the detected transition behind it is classified as coastline. This can also occur in coastal areas where coastlines are often backed by wetlands, resulting in an incorrect land–water boundary classified as coastline. For this reason, we implemented an outlier detection workflow, ensuring that significantly deviating observations are excluded from further analysis. This ensures that our coastline estimates for the entire coast of Suriname are on average within 50 m of the land–water boundary found across the heterogenous coastal landscape. Especially median annual coastline positions should therefore be used to analyse mid- to long-term coastline changes on a regional scale in a complex heterogenous mud-dominated landscape, where annual changes are frequently exceeding 30 m.

The difference in error estimates between the sites (Figure A5) also indicates that coastline indicators are not uniformly applicable along the Suriname coastline. Coastal stretches show differences in agreement between the observation and coastline proxies, suggesting that our method is not overly sensitive to different types of transitions between land and water that can naturally be found along the Suriname coastline. This indicates that the applied method can be used in heterogenous and complex landscapes for the consistent estimate of coastline positions.

False-positive detection of coastline position estimates, when the true coastline position is not visible, manifested due to the applied transect method. Especially when the morphology of the coastline is more complex or is not approximately aligned with the defined baseline, land–water transitions are falsely detected as coastline positions. For coastline detection we therefore included both temporal and spatial context to improve the accuracy of position estimates, by comparing the position with other position estimates on the transect within a time window. Rosner's outlier detection was chosen for its possibility of simultaneously detecting multiple outliers.

5.4 | Limitations and improvements

The standardized and objective end-member extraction technique applied here resulted in comparable estimates of mud abundance, useful to derive indications of subtidal mudbank presence and absence. Yet, due to image artefacts, cloud and shadow contamination, this estimated presence or absence required filtering and outlier detection. Most of the steps to do so required finetuning and parameterization to make the methodology applicable for the Suriname coastline. These steps ensure that: (1) spectral unmixing results are applied consistently; (2) cloud and shadow contamination is minimized; (3) bilateral filtering on the abundance maps is applied; (4) discontinuities along transects are consistently selected; and (5) annual changes in coastline positions, in relation to the presence or absence of mudbanks, are determined with reasonable accuracy.

Despite the implemented filtering steps, mudbanks were occasionally falsely detected (Figure 4). This is because automatically estimating the exact mudbank boundary locations is hampered by high sediment concentrations, related to high river discharges near river mouths and the observed natural variability in mud abundance. In order to optimize the parameterization of the workflow, it is therefore necessary to validate the mudbank positions with field observations. Consequently, it is necessary to determine the extent of mudbanks and simultaneously relate that to the extent of mudbanks that can be detected from remote sensing images (Zorrilla et al., 2018).

With respect to the estimated coastline positions, uncertainty in estimates is related to the observation frequency, obstruction of visibility by clouds and accuracy of the applied UDT, used here to separate land and water by means of Otsu thresholding. Only for the latter source of error is it possible to improve the accuracy by, for example, including the definition of sub-pixel coastlines (Pardo-Pascual et al., 2018) and the use of a water frequency index to perfect the estimation of the annual coastline position (Xu, 2018).

Although our coastline change analysis for Suriname quantified rates and directions of change with unprecedented spatial coverage and temporal resolution, further analysis can shed light on coastal system behaviour. This can be achieved by analysing mudbanks beyond the presence and absence estimates as presented in this paper. Demarcating mudbank footprints from observations with high temporal resolution can then shed light on migration rates, sediment storage and changes therein. When linked with information regarding other external forcing mechanisms like land use, wind data, coastline shape and morphology that govern the coastal dynamics in all the Guiana coast countries, it becomes possible to truly support decision-makers in their task to untangle subtleties in coastline behaviour for coastal wetlands. Variable responses of coastal ecosystems to ever-changing forcing mechanisms can then be incorporated in climate-resilient management strategies.

6 | CONCLUSIONS

By analysing all available Landsat images in our autonomous workflow, its temporal and spatial resolution are fully utilized to estimate, for the first time, coastline changes for the entire coast of Suriname between 1986 and 2020. These changes are then linked to the presence and absence of migrating subtidal mudbanks. We show that regional-scaled forcing mechanisms caused by these mudbanks have a strong imprint on the local coastline trajectories, with on average 32 m/yr accretion during mudbank presence and 4 m/yr erosion during mudbank absence. Yet, significant spatial and temporal variation in these trajectories exists on local scales. This suggests that linear and large-scale approaches to analyse annual to decadal coastline dynamics in Suriname, and other Guiana countries, should be handled with caution.

We reaffirm that currently at least six mudbanks are migrating along the coast of Suriname and that when mudbanks are present, coastal accretion or stabilization of erosion generally occurs. Due to the use of all available Landsat images, we are now also capable of showing where the effects of mudbanks are minimal or even opposite to what the conceptual mudbank model prescribes. This suggests it is evident that not every mudbank phase results in the same amount of coastal accretion at each location it passes, or alternatively not every interbank phase results in the same amount of coastal erosion.

These timescale dependencies might reflect combined effects of natural and anthropogenic factors that control both the mudbank and hydrodynamic forcing on the coast of Suriname, illustrating the difficulty of attributing all observed coastline changes to forcing imposed by mudbank migration alone. Although it is likely that mudbanks will continue to migrate alongshore in the decades to come, the variability in coastal morphology, sediment concentration and especially structural intervention (both anthropogenic and natural) will exert a complex influence on erosion and accretion of coastline positions. This implies that predictions of change for management purposes should be conducted with extreme care as they might create a false sense of security on short to medium timescales.

Our results further suggest that the potential for erosion during an interbank phase can be significantly larger than accretion rates in the mudbank phase before, especially when local settings including hydrodynamics, land use and other forms of anthropogenic interference are altered. This suggests that local coastal behaviour, not captured by linear rates of change, should be included in theoretical frameworks that are used to support decision-makers and coastal managers. For that purpose, quantitative information on coastline position changes from satellite observations spanning multiple decades are needed to supplement scattered, incomplete and poor-quality field observations and further refine modelling efforts that aim at predicting future changes in Suriname.

6.1 | SUPPLEMENTARY INFORMATION

Supplementary videos S1–S3 display the time series of coastline changes related to three selected transects displayed in Figure 8. Supplementary video S4 shows the spatiotemporal dimensions of coastline changes also found in the Hovmoller plot (Figure 6, panel a). For visualization purposes, the indication of mudbanks has been excluded in video S4.

AUTHOR CONTRIBUTIONS

JdV, **SdJ** and **BM** conceptualized the research; **SdJ**, **PV**, **BM** and **GR** acquired funding for the project; **JdV** developed the methodology, initiated data collection and investigation; **BM** and **SdJ** provided supervision; **JdV** wrote the initial draft and edited the final version; **BvM**, **GR**, **PV** and **SdJ** provided revision to the written drafts.

DATA AVAILABILITY STATEMENT

The pre-processing scripts that are used to define outliers for coastline position estimates and annual change metrics are available through Github: https://github.com/jobbo90/offshore_boundary/releases/tag/v0.2

The reported coastline position estimates and indications of mudbank presence can be found in the online GEE repository (v02), which also includes the scripts used to derive these indicators: https://code.earthengine.google.com/?accept_repo=users/jobdevries90/MangroMud

The UAV drone datasets used and/or analysed during the current study are available from the corresponding author on reasonable request.

ORCID

Job de Vries https://orcid.org/0000-0002-1332-8350
Barend van Maanen https://orcid.org/0000-0001-6115-5362
Gerben Ruessink https://orcid.org/0000-0001-9526-6087
Pita A. Verweij https://orcid.org/0000-0002-3577-2524
Steven M. de Jong https://orcid.org/0000-0002-1586-9601

REFERENCES

Alcântara, E., Barbosa, C., Stech, J., Novo, E. & Shimabukuro, Y. (2009) Improving the spectral unmixing algorithm to map water turbidity distributions. *Environmental Modelling and Software*, 24(9), 1051–1061. Available from: https://doi.org/10.1016/j.envsoft.2009.02.013

Allison, M.A. & Lee, M.T. (2004) Sediment exchange between Amazon mudbanks and shore-fringing mangroves in French Guiana. *Marine Geology*, 208(2–4), 169–190. Available from: https://doi.org/10.1016/j.margeo.2004.04.026

Allison, M.A., Lee, M.T., Ogston, A.S. & Aller, R.C. (2000) Origin of Amazon mudbanks along the northeastern coast of South America. *Marine Geology*, 163(1–4), 241–256. Available from: https://doi.org/10.1016/S0025-3227(99)00120-6

Allison, M.A., Nittrouer, C.A. & Faria, L.E.C. (1995) Rates and mechanisms of shoreface progradation and retreat downdrift of the Amazon river mouth. *Marine Geology*, 125(3–4), 373–392. Available from: https://doi.org/10.1016/0025-3227(95)00020-Y

Almonacid-Caballer, J., Sánchez-García, E., Pardo-Pascual, J.E., Balaguer-Beser, A.A. & Palomar-Vázquez, J. (2016) Evaluation of annual mean

shoreline position deduced from Landsat imagery as a mid-term coastal evolution indicator. *Marine Geology*, 372, 79–88. Available from: https://doi.org/10.1016/j.margeo.2015.12.015

Anthony, E.J., Brunier, G., Gardel, A., Hiwat, M., Cooper, A. & Fitzgerald, D. (2019) Chenier morphodynamics on the Amazon-influenced coast of Suriname, South America: Implications for beach ecosystem services. *Frontiers in Earth Science*, 7, 1–20. Available from: https://doi.org/10.3389/feart.2019.00035

Anthony, E.J., Dolique, F., Gardel, A., Gratiot, N., Proisy, C. & Polidori, L. (2008) Nearshore intertidal topography and topographic-forcing mechanisms of an Amazon-derived mud bank in French Guiana. *Continental Shelf Research*, 28(6), 813–822. Available from: https://doi.org/10.1016/j.csr.2008.01.003

Anthony, E.J., Gardel, A. & Gratiot, N. (2013) Fluvial sediment supply, mud banks, cheniers and the morphodynamics of the coast of South America between the Amazon and Orinoco river mouths. *Geological Society of London, Special Publications*, 388(1), 533–560. Available from: https://doi.org/10.1144/sp388.8

Anthony, E.J., Gardel, A., Gratiot, N., Proisy, C., Allison, M.A., Dolique, F. & Fromard, F. (2010) The Amazon-influenced muddy coast of South America: A review of mud–bank–shoreline interactions. *Earth-Science Reviews*, 103(3–4), 99–121. Available from: https://doi.org/10.1016/j.earscirev.2010.09.008

Anthony, E.J., Gardel, A., Proisy, C., Fromard, F., Gensac, E., Peron, C., Walcker, R. & Lesourd, S. (2013) The role of fluvial sediment supply and river-mouth hydrology in the dynamics of the muddy, Amazon-dominated Amapá-Guianas coast, South America: A three-point research agenda. *Journal of South American Earth Sciences*, 44, 18–24. Available from: https://doi.org/10.1016/j.jsames.2012.06.005

Asokan, A. & Anitha, J. (2020) Adaptive Cuckoo Search based optimal bilateral filtering for denoising of satellite images. *ISA Transactions*, 100, 308–321. Available from: https://doi.org/10.1016/j.isatra.2019.11.008

Augustinus, P.G.E.F. (1989) Cheniers and chenier plains: A general introduction. *Marine Geology*, 90(4), 219–229. Available from: https://doi.org/10.1016/0025-3227(89)90126-6

Augustinus, P.G.E.F. (2004) The influence of the trade winds on the coastal development of the Guianas at various scale levels: A synthesis. *Marine Geology*, 208(2–4), 145–151. Available from: https://doi.org/10.1016/j.margeo.2004.04.007

Augustinus, P.G.E.F., Hazelhoff, L. & Kroon, A. (1989) The chenier coast of Suriname: Modern and geological development. *Marine Geology*, 90(4), 269–281. Available from: https://doi.org/10.1016/0025-3227(89)90129-1

Baghdadi, N., Gratiot, N., Lefebvre, J.-P., Oliveros, C. & Bourguignon, A. (2004) Coastline and mudbank monitoring in French Guiana: Contributions of radar and optical satellite imagery. *Canadian Journal of Remote Sensing*, 30(2), 109–122. Available from: https://doi.org/10.5589/m03-059

Balke, T., Bouma, T.J., Horstman, E.M., Webb, E.L., Erftemeijer, P.L.A. & Herman, P.M.J. (2011) Windows of opportunity: Thresholds to mangrove seedling establishment on tidal flats. *Marine Ecology Progress Series*, 440, 1–9. Available from: https://doi.org/10.3354/meps09364

Baltzer, F., Allison, M.A. & Fromard, F. (2004) Material exchange between the continental shelf and mangrove-fringed coasts with special reference to the Amazon-Guianas coast. *Marine Geology*, 208(2–4), 115–126. Available from: https://doi.org/10.1016/j.margeo.2004.04.024

Boak, E.H. & Turner, I.L. (2005) Shoreline definition and detection: A review. *Journal of Coastal Research*, 21, 688–703. Available from: https://doi.org/10.2112/03-0071.1

Brunier, G., Fleury, J., Anthony, E.J., Gardel, A. & Dussouillez, P. (2016) Close-range airborne Structure-from-Motion photogrammetry for high-resolution beach morphometric surveys: Examples from an embayed rotating beach. *Geomorphology*, 261, 76–88. Available from: https://doi.org/10.1016/j.geomorph.2016.02.025

Carbonneau, P.E. & Dietrich, J.T. (2017) Cost-effective non-metric photogrammetry from consumer-grade sUAS: Implications for direct georeferencing of structure from motion photogrammetry. *Earth Surface Processes and Landforms*, 42(3), 473–486. Available from: https://doi.org/10.1002/esp.4012

Chevalier, C., Froidefond, J.-M. & Devenon, J.-L. (2008) Numerical analysis of the combined action of littoral current, tide and waves on the suspended mud transport and on turbid plumes around French Guiana mudbanks. *Continental Shelf Research*, 28(4–5), 545–560. Available from: https://doi.org/10.1016/j.csr.2007.09.011

de Jong, S.M., Shen, Y., de Vries, J., Bijnaar, G., van Maanen, B., Augustinus, P. & Verweij, P. (2021) Mapping mangrove dynamics and colonization patterns at the Suriname coast using historic satellite data and the LandTrendr algorithm. *International Journal of Applied Earth Observation and Geoinformation*, 97, 102293. Available from: https://doi.org/10.1016/j.jag.2020.102293

de Vries, J., van Maanen, B., Ruessink, G., Verweij, P.A. & de Jong, S.M. (2021) Unmixing water and mud: Characterizing diffuse boundaries of subtidal mud banks from individual satellite observations. *International Journal of Applied Earth Observation and Geoinformation*, 95, 102252. Available from: https://doi.org/10.1016/j.jag.2020.102252

Dolan, R., Fenster, M.S. & Holme, S.J. (1991) Temporal analysis of shoreline recession and accretion. *Journal of Coastal Research*, 7, 723–744.

Donchyts, G., Baart, F., Winsemius, H.C., Gorelick, N., Kwadijk, J. & van de Giesen, N. (2016) Earth's surface water change over the past 30 years. *Nature Climate Change*, 6(9), 810–813. Available from: https://doi.org/10.1038/nclimate3111

Eisma, D. & van der Marel, H.W.M. (1971) Marine muds along the Guyana coast and their origin from the Amazon basin. *Contributions to Mineralogy and Petology*, 31(4), 321–334. Available from: https://doi.org/10.1007/BF00371152

Ellison, J.C. (2015) Vulnerability assessment of mangroves to climate change and sea-level rise impacts. *Wetlands Ecology and Management*, 23(2), 115–137. Available from: https://doi.org/10.1007/s11273-014-9397-8

Friess, D.A., Krauss, K.W., Horstman, E.M., Balke, T., Bouma, T.J., Galli, D. & Webb, E.L. (2012) Are all intertidal wetlands naturally created equal? Bottlenecks, thresholds and knowledge gaps to mangrove and saltmarsh ecosystems. *Biological Reviews*, 87(2), 346–366. Available from: https://doi.org/10.1111/j.1469-185X.2011.00198.x

Froidefond, J.M., Pujos, M. & Andre, X. (1988) Migration of mud banks and changing coastline in French Guiana. *Marine Geology*, 84(1–2), 19–30. Available from: https://doi.org/10.1016/0025-3227(88)90122-3

Fromard, F., Vega, C. & Proisy, C. (2004) Half a century of dynamic coastal change affecting mangrove shorelines of French Guiana: A case study based on remote sensing data analyses and field surveys. *Marine Geology*, 208(2–4), 265–280. Available from: https://doi.org/10.1016/j.margeo.2004.04.018

Gardel, A. & Gratiot, N. (2005) A satellite image-based method for estimating rates of mud bank migration, French Guiana, South America. *Journal of Coastal Research*, 214, 720–728. Available from: https://doi.org/10.2112/03-0100.1

Gardel, A. & Gratiot, N. (2006) Monitoring of coastal dynamics in French Guiana from 16 years of SPOT satellite images. *Journal of Coastal Research*, 3, 1502–1505.

Gensac, E., Lesourd, S., Gardel, A., Anthony, E.J., Proisy, C. & Loisel, H. (2011) Short-term prediction of the evolution of mangrove surface areas: The example of the mud banks of Kourou and Sinnamary, French Guiana. *Journal of Coastal Research*, 214, 388–392.

Gorelick, N., Hancher, M., Dixon, M., Ilyushchenko, S., Thau, D. & Moore, R. (2017) Google Earth Engine: Planetary-scale geospatial analysis for everyone. *Remote Sensing of Environment*, 202, 18–27. Available from: https://doi.org/10.1016/j.rse.2017.06.031

Gratiot, N., Anthony, E.J., Gardel, A., Gaucherel, C., Proisy, C. & Wells, J.T. (2008) Significant contribution of the 18.6 year tidal cycle to regional coastal changes. *Nature Geoscience*, 1(3), 169–172. Available from: https://doi.org/10.1038/ngeo127

Gratiot, N., Gardel, A. & Anthony, E.J. (2007) Trade-wind waves and mud dynamics on the French Guiana coast, South America: Input from ERA-40 wave data and field investigations. *Marine Geology*, 236(1–2), 15–26. Available from: https://doi.org/10.1016/j.margeo.2006.09.013

Housman, I.W., Chastain, R.A. & Finco, M.V. (2018) An evaluation of forest health insect and disease survey data and satellite-based remote sensing forest change detection methods: Case studies in the

United States. *Remote Sensing*, 10(8), 1184. Available from: https://doi.org/10.3390/rs10081184

Kirwan, M.L. & Megonigal, J.P. (2013) Tidal wetland stability in the face of human impacts and sea-level rise. *Nature*, 504, 53–60.

Klemas, V. (2013) Remote sensing of emergent and submerged wetlands: An overview. *International Journal of Remote Sensing*, 34(18), 6286–6320. Available from: https://doi.org/10.1080/01431161.2013.800656

Lefebvre, J.-P.P., Dolique, F. & Gratiot, N. (2004) Geomorphic evolution of a coastal mudflat under oceanic influences: An example from the dynamic shoreline of French Guiana. *Marine Geology*, 208(2–4), 191–205. Available from: https://doi.org/10.1016/j.margeo.2004.04.008

Li, W. & Gong, P. (2016) Continuous monitoring of coastline dynamics in western Florida with a 30-year time series of Landsat imagery. *Remote Sensing of Environment*, 179, 196–209. Available from: https://doi.org/10.1016/j.rse.2016.03.031

Liu, H. & Jezek, K.C. (2004) Automated extraction of coastline from satellite imagery by integrating Canny edge detection and locally adaptive thresholding methods. *International Journal of Remote Sensing*, 25(5), 937–958. Available from: https://doi.org/10.1080/0143116031000139890

Lu, S., Wu, B., Yan, N. & Wang, H. (2011) Water body mapping method with HJ-1A/B satellite imagery. *International Journal of Applied Earth Observation and Geoinformation*, 13(3), 428–434. Available from: https://doi.org/10.1016/j.jag.2010.09.006

Luijendijk, A.P., Hagenaars, G., Ranasinghe, R., Baart, F., Donchyts, G. & Aarninkhof, S. (2018) The state of the world's beaches. *Scientific Reports*, 8(1), 1-11. Available from: https://doi.org/10.1038/s41598-018-24630-6

McFeeters, S.K. (1996) The use of the Normalized Difference Water Index (NDWI) in the delineation of open water features. *International Journal of Remote Sensing*, 17(7), 1425–1432. Available from: https://doi.org/10.1080/01431169608948714

Millard, S.P. (2014) *EnvStats: An R Package for Environmental Statistics*. New York: Springer. https://doi.org/10.1002/9780470057339.vae043.pub2

Mondal, P., Trzaska, S. & de Sherbinin, A. (2018) Landsat-derived estimates of mangrove extents in the Sierra Leone coastal landscape complex during 1990–2016. *Sensors*, 18(1), 12. Available from: https://doi.org/10.3390/s18010012

Moore, L.J., Ruggiero, P. & List, J.H. (2006) Comparing mean high water and high water line shorelines: Should prosy-datum offsets be incorporated into shoreline change analysis? *Journal of Coastal Research*, 22, 894–905. Available from: https://doi.org/10.2112/04-0401.1

Nijbroek, R. (2014) Mangroves, mudbanks and seawalls: Whose environmental knowledge counts when adapting to sea level rise in Suriname? *Journal of Political Ecology*, 21, 533–550. Available from: https://doi.org/10.1016/0037

Odermatt, D., Gitelson, A., Ernesto, V., Schaepman, M.E., Brando, V.E., Schaepman, M.E., Ernesto, V. & Schaepman, M.E. (2012) Review of constituent retrieval in optically deep and complex waters from satellite imagery. *Remote Sensing of Environment*, 118, 116–126. Available from: https://doi.org/10.1016/j.rse.2011.11.013

Orseau, S., Zorrilla, N.A., Huybrechts, N., Lesourd, S. & Gardel, A. (2020) Decadal-scale morphological evolution of a muddy open coast. *Marine Geology*, 420, 106048. Available from: https://doi.org/10.1016/j.margeo.2019.106048

Osland, M.J., Feher, L.C., Griffith, K.T., Cavanaugh, K.C., Enwright, N.M., Day, R.H., Stagg, C.L., Krauss, K.W., Howard, R.J., Grace, J.B. & Rogers, K. (2017) Climatic controls on the global distribution, abundance, and species richness of mangrove forests. *Ecological Monographs*, 87(2), 341–359. Available from: https://doi.org/10.1002/ecm.1248

Pardo-Pascual, J.E., Almonacid-Caballer, J., Ruiz, L.A. & Palomar-Vázquez, J. (2012) Automatic extraction of shorelines from Landsat TM and ETM+ multi-temporal images with subpixel precision. *Remote Sensing of Environment*, 123, 1–11. Available from: https://doi.org/10.1016/j.rse.2012.02.024

Pardo-Pascual, J.E., Sánchez-García, E., Almonacid-Caballer, J., Palomar-Vázquez, J.M., de los Santos, E.P., Fernández-Sarría, A.,

Balaguer-Beser, Á. & Elena, S. (2018) Assessing the accuracy of automatically extracted shorelines on microtidal beaches from Landsat 7, Landsat 8 and Sentinel-2 imagery. *Remote Sensing*, 10(2), 1–20. Available from: https://doi.org/10.3390/rs10020326

Plaziat, J.C. & Augustinus, P.G.E.F. (2004) Evolution of progradation/erosion along the French Guiana mangrove coast: A comparison of mapped shorelines since the 18th century with Holocene data. *Marine Geology*, 208(2–4), 127–143. Available from: https://doi.org/10.1016/j.margeo.2004.04.006

Proisy, C., Gratiot, N., Anthony, E.J., Gardel, A., Fromard, F. & Heuret, P. (2009) Mud bank colonization by opportunistic mangroves: A case study from French Guiana using lidar data. *Continental Shelf Research*, 29(3), 632–641. Available from: https://doi.org/10.1016/j.csr.2008.09.017

Proisy, C., Walcker, R., Blanchard, E., Gardel, A. & Anthony, E.J. (2021) Mangroves: A natural early-warning system of erosion on open muddy coasts in French Guiana. In: Sidik, F. & Friess, D.A. (Eds.) *Dynamic Sedimentary Environments of Mangrove Coasts*, Vol. 47–66. Amsterdam: Elsevier. https://doi.org/10.1016/b978-0-12-816437-2.00011-2

Pujos, M. & Froidefond, J.-M. (1995) Water masses and suspended matter circulation on the French Guiana continental shelf. *Continental Shelf Research*, 15(9), 1157–1171. Available from: https://doi.org/10.1016/0278-4343(94)00062-R

Rine, J.M. & Ginsburg, R.N. (1985) Depositional facies of a mud shoreface in Suriname, South America – a mud analogue to sandy shallow-marine deposits. *Journal of Sedimentary Petrology*, 55, 633–652. Available from: https://doi.org/10.1306/212F87A6-2B24-11D7-8648000102C1865D

Rosner, B. (1983) Percentage points for a generalized ESD many-outlier procedure. *Technometrics*, 25(2), 165–172. Available from: https://doi.org/10.1080/00401706.1983.10487848

Samiksha, S.V., Vethamony, P., Rogers, W.E., Pednekar, P.S., Babu, M.T. & Dineshkumar, P.K. (2017) Wave energy dissipation due to mudbanks formed off southwest coast of India. *Estuarine, Coastal and Shelf Science*, 196, 387–398. Available from: https://doi.org/10.1016/j.ecss.2017.07.018

Stive, M.J.F., Aarninkhof, S.G.J., Hamm, L., Hanson, H., Larson, M., Wijnberg, K.M., Nicholls, R.J. & Capobianco, M. (2002) Variability of shore and shoreline evolution. *Coastal Engineering*, 47(2), 211–235. Available from: https://doi.org/10.1016/S0378-3839(02)00126-6

Taylor, K.H. & Purkis, S.J. (2012) Evidence for the southward migration of mud banks in Florida Bay. *Marine Geology*, 311–314, 52–56. Available from: https://doi.org/10.1016/j.margeo.2012.04.007

Tomasi, C. & Manduchi, R. (1998) Bilateral filtering for gray and color images. In: *Proceedings of the 1998 IEEE International Conference on Computer Vision*. New York: IEEE, pp. 839–846 https://doi.org/10.1109/iccv.1998.710815

Toorman, E.A., Anthony, E.J., Augustinus, P.G.E.F., Gardel, A., Gratiot, N., Homenauth, O., Huybrechts, N. & Monbaliu, J. (2018) Interaction of mangroves, coastal hydrodynamics, and morphodynamics along the coastal fringes of the Guianas. *Coastal Research Library*, 25, 429–473. Available from: https://doi.org/10.1007/978-3-319-73016-5_20

Tucker, C.J. (1979) Red and photographic infrared linear combinations for monitoring vegetation. *Remote Sensing of Environment*, 2(2), 127–150. Available from: https://doi.org/10.1016/0034-4257(79)90013-0

Vantrepotte, V., Gensac, E., Loisel, H., Gardel, A., Dessailly, D. & Mériaux, X. (2013) Satellite assessment of the coupling between in water suspended particulate matter and mud banks dynamics over the French Guiana coastal domain. *Journal of South American Earth Sciences*, 44, 25–34. Available from: https://doi.org/10.1016/j.jsames.2012.11.008

Vos, K., Harley, M.D., Splinter, K.D., Simmons, J.A. & Turner, I.L. (2019) Sub-annual to multi-decadal shoreline variability from publicly available satellite imagery. *Coastal Engineering*, 150, 160–174. Available from: https://doi.org/10.1016/j.coastaleng.2019.04.004

Walcker, R., Anthony, E.J., Cassou, C., Aller, R.C., Gardel, A., Proisy, C., Martinez, J.M. & Fromard, F. (2015) Fluctuations in the extent of mangroves driven by multi-decadal changes in North Atlantic waves. *Journal of Biogeography*, 42(11), 2209–2219. Available from: https://doi.org/10.1111/jbi.12580

Wells, J.T. & Coleman, J.M. (1981a) Physical processes and fine-grained sediment dynamics, coast of Surinam, South America. *Journal of Sedimentary Research*, 51, 1053-1068. Available from: https://doi.org/10.1306/212F7E1E-2B24-11D7-8648000102C1865D

Wells, J.T. & Coleman, J.M. (1981b) Periodic mudflat progradation, northeastern coast of South America: A hypothesis. *Journal of Sedimentary Petrology*, 51(4), 1069–1075. Available from: https://doi.org/10.2110/jsr.51.1069

Westoby, M.J., Brasington, J., Glasser, N.F., Hambrey, M.J. & Reynolds, J.M. (2012) "Structure-from-Motion" photogrammetry: A low-cost, effective tool for geoscience applications. *Geomorphology*, 179, 300–314. Available from: https://doi.org/10.1016/j.geomorph.2012.08.021

Willems, T., De Backer, A., Wan Tong You, K., Vincx, M. & Hostens, K. (2015) Spatio-temporal distribution patterns of the epibenthic community in the coastal waters of Suriname. *Continental Shelf Research*, 108, 25–40. Available from: https://doi.org/10.1016/j.csr.2015.08.006

Winterwerp, J.C., Graaff, R.F.D., Groeneweg, J. & Luijendijk, A.P. (2007) Modelling of wave damping at Guyana mud coast. *Coastal Engineering*, 54(3), 249–261. Available from: https://doi.org/10.1016/j.coastaleng.2006.08.012

Woodroffe, C.D., Rogers, K., McKee, K.L., Lovelock, C.E., Mendelssohn, I.A. & Saintilan, N. (2016) Mangrove sedimentation and response to relative sea-level rise. *Annual Review of Marine Science*, 8(1), 243–266. Available from: https://doi.org/10.1146/annurev-marine-122414-034025

Xie, D., Schwarz, C., Brückner, M.Z.M. & Kleinhans, M.G. (2020) Mangrove diversity loss under sea-level rise triggered by bio-morphodynamic feedbacks and anthropogenic pressures. *Environmental Research Letters*, 15(11), 114033. Available from: https://doi.org/10.1088/1748-9326/abc122

Xu, N. (2018) Detecting coastline change with all available Landsat data over 1986–2015: A case study for the state of Texas, USA. *Atmosphere*, 9(3), 107. Available from: https://doi.org/10.3390/atmos9030107

Zorrilla, N.A., Vantrepotte, V., Gensac, E., Huybrechts, N. & Gardel, A. (2018) The advantages of Landsat 8 OLI-derived suspended particulate matter maps for monitoring the subtidal extension of Amazonian coastal mud banks (French Guiana). *Remote Sensing*, 10(11), 1–17. Available from: https://doi.org/10.3390/rs10111733

SUPPORTING INFORMATION

Additional supporting information may be found in the online version of the article at the publisher's website.
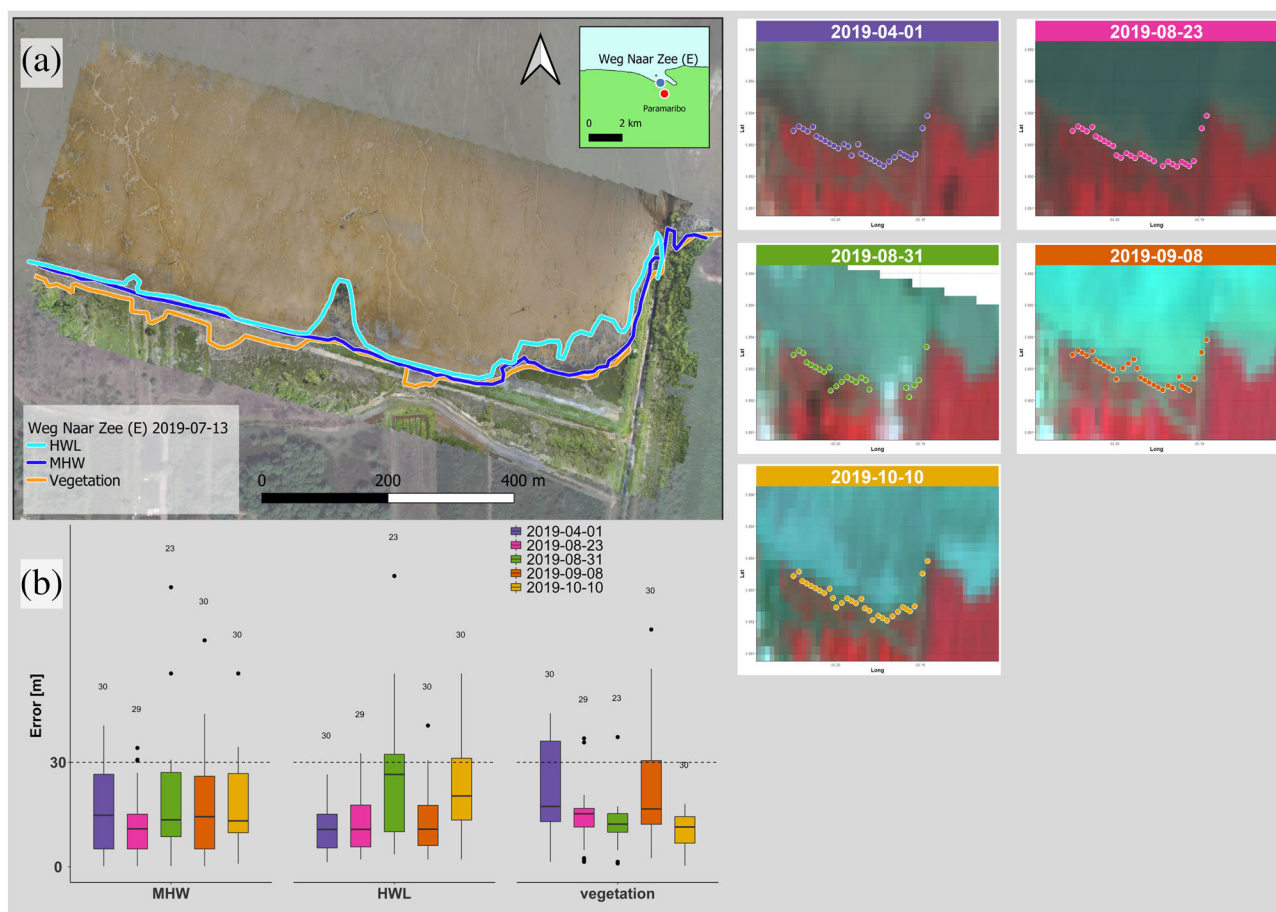
APPENDIX A

FIGURE A1 Validation results of the Landsat images acquired within 100 days of collecting the high-resolution UAV images near Weg Naar Zee east (2019-07-13). Only Landsat images are shown on the right that are not obstructed from sight by clouds or missing data. Panel A shows the digitized shorelines in the UAV image that are used for validation. The panels on the right show the different Landsat images that were used, together with the automatically derived shoreline positions. The coloured boxplots in panel B summarize the difference for each of these Landsat-derived shoreline positions compared to the different digitized shoreline positions visible in panel A (MHW, HWL and vegetation interface). The Landsat 7 image acquired at 2019-08-31 is an example that illustrates missing data-related SLC-off striping
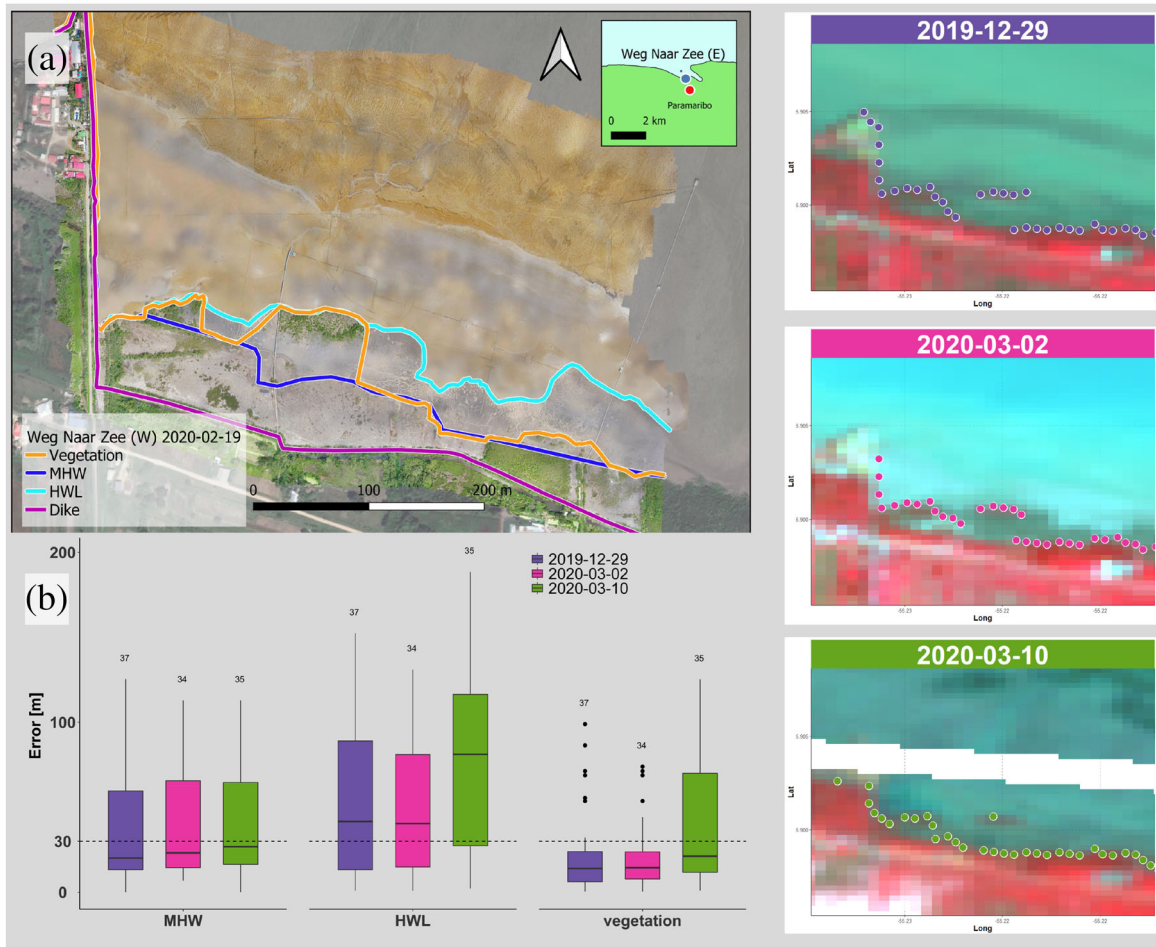
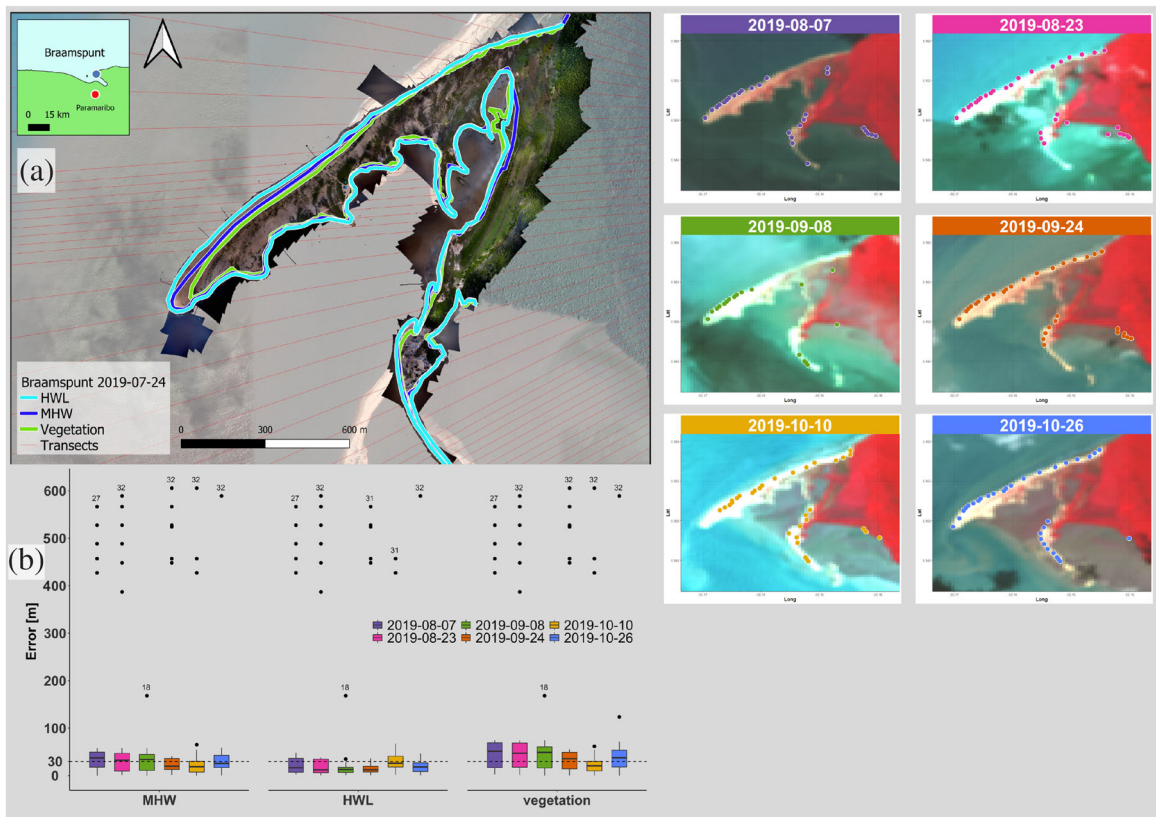**FIGURE A2** Same as Figure A1 but now for Weg Naar Zee west in 2020

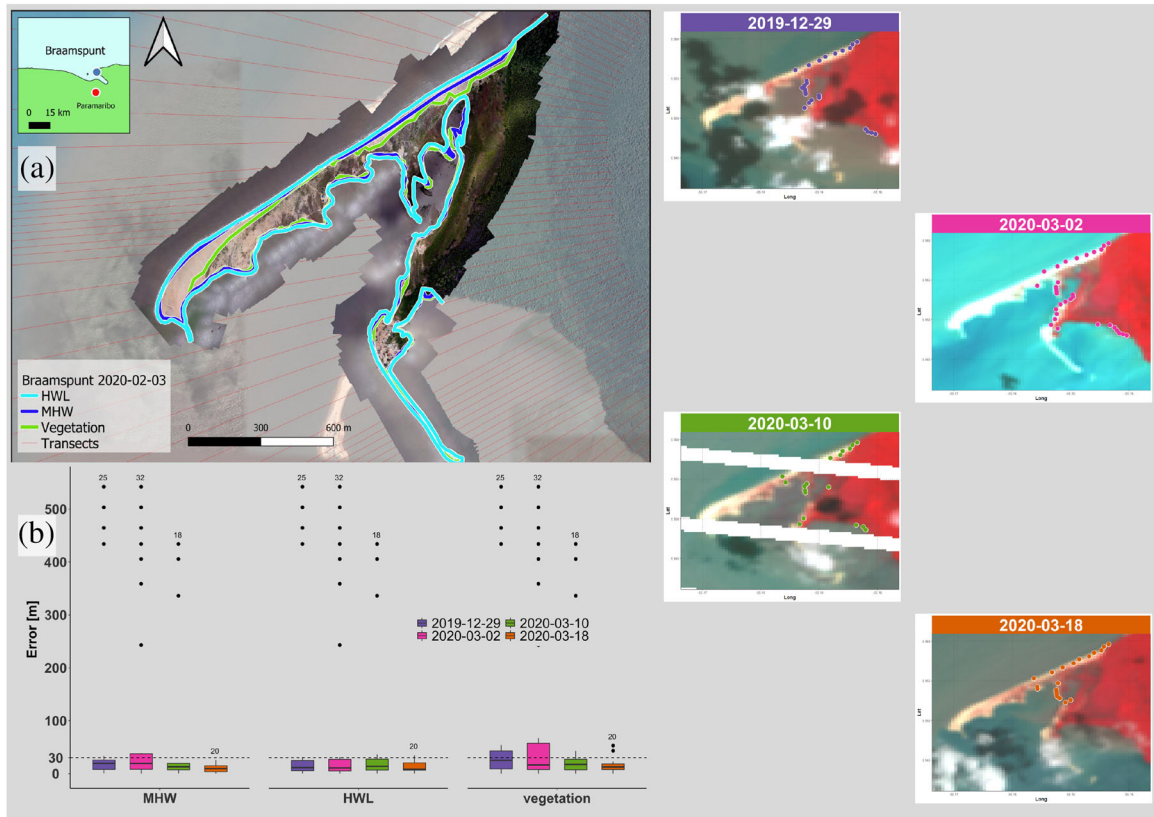**FIGURE A3** Same as Figure A1 but now for Braamspunt in 2019

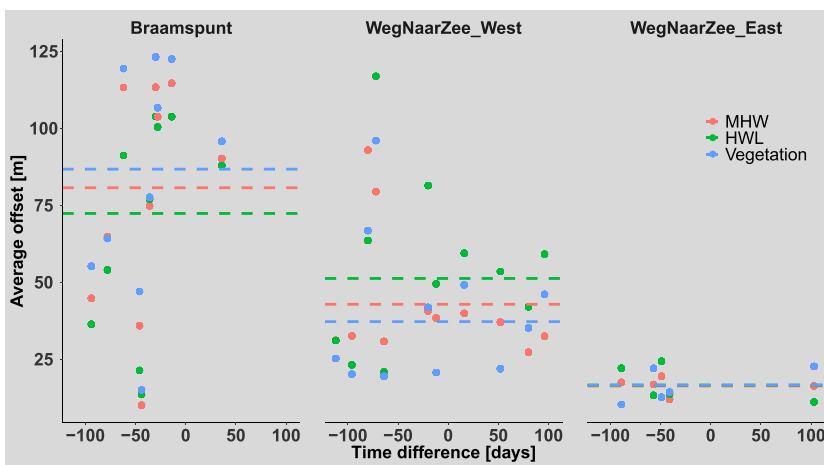**FIGURE A4** Same as Figure A1 but now for Braamspunt in 2020

FIGURE A5 Average offset between Landsat position estimates and the different coastline proxies from UAV orthophotos. The average offset on the *y*-axis is linked to the acquisition date of the corresponding Landsat image, defined as the number of days it differs from the acquisition of the UAV image (*x*-axis). The dots represent mean offsets, computed for each Landsat observation compared to the selected coastline proxy in each UAV image. The dashed lines correspond to the overall mean offset of all position estimates from the used Landsat observations, separated for the different coastline proxies used in this analysis
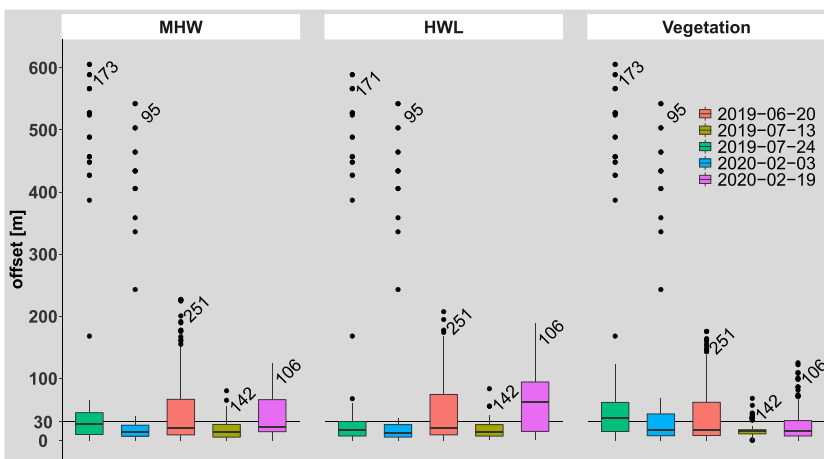

FIGURE A6 Variability accuracy for the different coastline proxies defined in the selected UAV orthophotos. Each boxplot compromises all Landsat position estimates that are compared to the coastline proxies as defined in the different UAV images. The acquisitions over Braamspunt (2019-07-24 and 2020-02-03) contain relatively more and larger outliers compared to the acquisition over Weg Naar Zee. Especially, the acquisitions at Weg Naar Zee west (2019-06-20 and 2020-02-19) have a relatively large offset between the coastline position estimates and the different coastline indicators, which can be related to the more complex and heterogenous coastal morphology